Aus der Klinik und Poliklinik für Nuklearmedizin
Klinikum der Ludwig-Maximilians-Universität München
Direktor: Univ.-Prof. Dr. med. Rudolf Werner

Impact of Temporal Sampling and Motion-Induced Errors on Clinical Strategies for SPECT-Based Dosimetry in ^{177}Lu-PSMA Therapy of Advanced Prostate Cancer

Dissertation
zum Erwerb des Doktorgrades der Naturwissenschaften
an der Medizinischen Fakultät der
Ludwig–Maximilians–Universität München

vorgelegt von
Sandra Resch
aus
Rotthalmünster

2025

Mit Genehmigung der Medizinischen Fakultät
der Ludwig–Maximilians–Universität München

Betreuer:	Prof. Dr. Guido Böning
Zweitgutachter:	PD Dr. Christian Thieke
Dekan:	Prof. Dr. med. Thomas Gudermann
Tag der mündlichen Prüfung:	26. Februar 2026

Eidesstattliche Versicherung

Resch, Sandra

Name, Vorname

Ich erkläre hiermit an Eides statt,

dass ich die vorliegende Dissertation mit dem Titel

Impact of Temporal Sampling and Motion-Induced Errors on Clinical Strategies for SPECT-Based Dosimetry in ^{177}*Lu-PSMA Therapy of Advanced Prostate Cancer*

selbständig verfasst, mich außer der angegebenen keiner weiteren Hilfsmittel bedient und alle Erkenntnisse, die aus dem Schrifttum ganz oder annähernd übernommen sind, als solche kenntlich gemacht habe und nach ihrer Herkunft unter Bezeichnung der Fundstelle einzeln nachgewiesen habe.

Ich erkläre des Weiteren, dass die hier vorgelegte Dissertation nicht in gleicher oder in ähnlicher Form bei einer anderen Stelle zur Erlangung eines akademischen Grades eingereicht wurde.

München, 14.05.2025	Sandra Resch
Ort, Datum	Unterschrift

LUDWIG-
MAXIMILIANS-
UNIVERSITÄT
MÜNCHEN

Dekanat Medizinische Fakultät
Promotionsbüro

Erklärung zur Übereinstimmung der gebundenen Ausgabe der Dissertation mit der elektronischen Fassung

Resch, Sandra

Name, Vorname

Hiermit erkläre ich, dass die elektronische Version der eingereichten Dissertation mit dem Titel:

Impact of Temporal Sampling and Motion-Induced Errors on Clinical Strategies for SPECT-Based Dosimetry in 177-Lu-PSMA Therapy of Advanced Prostate Cancer

in Inhalt und Formatierung mit den gedruckten und gebundenen Exemplaren übereinstimmt.

München, 14.05.2025

Ort, Datum

Sandra Resch

Unterschrift Doktorandin/Doktorand

Contents

List of Abbreviations

PSMA	Prostate-specific membrane antigen
SPECT	Single photon emission computed tomography
mCRPC	Metastatic castration-resistant prostate cancer
FDA	U.S. Food and Drug Administration and European Medicines Agency
EMA	European Medicines Agency
PET	Positron emission computed tomography
SPECT/CT	Single photon emission computed tomography
OSEM	Ordered-subset expectation maximization
MLEM	Maximum-likelihood-expectation-maximization
MAP	Maximum-a-posteriori
RC	Recovery coefficient
PVC	Partial volume correction
VOI	Volume(s) of interest
p.i.	Post-injection
MIRD	Medical Internal Radiation Dose
STP	Single time point
SUV	Standardized uptake value
TAC	Time activity curve
TIA	Time integrated activity
SSB	Single-strand break
DSB	Double-strand break
RBE	Relative biological effectiveness
LET	Linear energy transfer
BED	Biologically effective dose
LQ	Linear-quadratic
SIRT	Selective internal radiation therapy
CZT	Cadmium Zinc Telluride
AI	Artificial intelligence

List of Publications

Original Publications

The following two original publications are subject of this cumulative dissertation in accordance with the promotion regulation for natural sciences of the medical faculty of Ludwig-Maximilians-University Munich.

S. Resch, S. Takayama Fouladgar, M. Zacherl, G.T. Sheikh, G. Liubchenko, M. Rumiantcev, L.M. Unterrainer, V. Wenter, P. Bartenstein, S.I. Ziegler, H. Ilhan, L. Beyer, G. Böning, & A. Delker, "Investigation of image-based lesion and kidney dosimetry protocols for ^{177}Lu-PSMA-I&T therapy with and without a late SPECT/CT acquisition", *EJNMMI physics*, vol. 10, no. 1, p. 11, 2023.

S. Resch, S.I. Ziegler, G. Sheikh, L.M. Unterrainer, M.J. Zacherl, P. Bartenstein, Böning G., J. Brosch-Lenz & A. Delker, "Impact of the Reference Multiple-Time-Point Dosimetry Protocol on the Validity of Single-Time-Point Dosimetry for ^{177}Lu-PSMA-I&T Therapy", *Journal of Nuclear Medicine*, vol. 65, no. 8, pp. 1272–1278, 2024.

Additional Publications

I contributed to the following publications as a co-author while pursuing my dissertation at the medical faculty of Ludwig-Maximilians-University Munich.

M. Rumiantcev, W.B. Li, S. Lindner, G. Liubchenko, **S. Resch**, P. Bartenstein, S.I. Ziegler, G. Böning & A. Delker, "Estimation of relative biological effectiveness of ^{225}Ac compared to ^{177}Lu during [^{225}Ac] Ac-PSMA and [^{177}Lu] Lu-PSMA radiopharmaceutical therapy using TOPAS/TOPAS-nBio/MEDRAS", *EJNMMI physics*, vol. 10, no. 1, p. 53, 2023.

G. Liubchenko, G. Böning, M. Zacherl, M. Rumiantcev, L.M. Unterrainer, F.J. Gildehaus, M. Brendel, **S. Resch**, P. Bartenstein, S.I. Ziegler & A. Delker, "Image-based dosimetry for [^{225}Ac] Ac-PSMA-I&T therapy and the effect of daughter-specific pharmacokinetics", *European Journal of Nuclear Medicine and Molecular Imaging*, vol. 51, no. 8, pp. 2504-2514, 2024.

A. Delker, M. Schleske, G. Liubchenko, I. Berg, M.J. Zacherl, M. Brendel, F.J. Gildehaus, M. Rumiantcev, **S. Resch**, K. Hürkamp, V. Wenter, L.M. Unterrainer, P. Bartenstein, S.I. Ziegler, L. Beyer & G. Böning, "Biodistribution and dosimetry for combined [^{177}Lu] Lu-PSMA-I&T/[^{225}Ac] Ac-PSMA-I&T therapy using multi-isotope quantitative SPECT imaging", *European Journal of Nuclear Medicine and Molecular Imaging*, vol. 50, no. 5, pp. 1280-1290, 2023.

Conference Abstracts

I contributed with the following abstracts, presentations and/or posters to scientific conferences while pursuing my dissertation at the medical faculty of Ludwig-Maximilians-University Munich.

S. Resch, S.L. Takayama Fouladgar, G.T. Sheikh, G. Liubchenko, M. Rumiantcev, M. Zacherl, V. Wenter, P. Bartenstein, S.I. Ziegler, H. Ilhan, L. Beyer, G. Böning, & A. Delker, "Influence of a late SPECT/CT acquisition and the selected fit model on lesion dosimetry for Lu-177-PSMA-I&T therapy in the context of clinical routine", *European Journal of Nuclear Medicine and Molecular Imaging*, vol. 49, Suppl. 1, p. 643, 2022.

S. Resch, G. Liubchenko, M. Rumiantcev, M. Zacherl, G.T. Sheikh, V. Wenter, P. Bartenstein, S.I. Ziegler, G. Böning & A. Delker, "Vergleich verschiedener Methoden zur Einzelzeitpunktdosimetrie bei der 177Lu-PSMA Therapie in Abhängigkeit von Gewebetyp und Referenzmodell", *Nuklearmedizin*, vol. 62, no. 02, p. L32, 2023.

S. Resch, X. Shen, M. Reymann, F. Basi Massanes, P. Bartenstein, G. Platsch, A.H. Vija, G. Böning & A. Delker, "Impact Of Small Patient Motion During SPECT/CT Scans Onto Activity Quantification Of 177Lu-PSMA Based on A Phantom Simulation", *European Journal of Nuclear Medicine and Molecular Imaging*, vol. 50, no. 1, p. 373, 2023.

S. Resch, X. Shen, M. Reymann, F. Basi Massanes, P. Bartenstein, G. Platsch, A.H. Vija, G. Böning & A. Delker, "Einfluss von kleinen Patientenbewegungen während SPECT/CT Scans auf die Aktivitätsquantifizierung von 177Lu-PSMA basierend auf einer Phantom-Simulation", *Nuklearmedizin*, vol. 63, no. 02, p. 03, 2024.

S. Resch, M. Rumiantcev, X. Shen, G. Liubchenko, S.I. Ziegler, G. Böning & A. Delker, "Impact of small patient motion during ^{177}Lu-PSMA SPECT/CT scans onto lesion dosimetry based on a phantom simulation study", *Physica Medica*, vol. 125, p. 103874, 2024.

S. Resch, M. Rumiantcev, G. Liubchenko, M. Brendel, S.I. Ziegler, G. Böning & A. Delker, "Influence of patient motion on image-based dosimetry for 177 Lu-PSMA therapy", *European Journal of Nuclear Medicine and Molecular Imaging*, vol. 51, p. 211, 2024.

Abstract

Aim

SPECT-based dosimetry for ^{177}Lu-PSMA radioligand therapy in patients with metastatic prostate cancer is not only necessary to monitor the absorbed dose to organs-at-risk, but also important to make progress in establishing and understanding dose-response relationships and to move toward personalized radionuclide therapies. However, the high clinical workload, cost and patient burden associated with the large number of SPECT scans required make it difficult to establish routine clinical dosimetry. In addition, SPECT-based dosimetry is prone to error due to uncertainties in image-based activity quantification. As prostate cancer patients often suffer from severe bone pain, irregular patient motion during long scans is an important issue in SPECT quantification, but has not yet been addressed for dosimetry purposes. The aim of this dissertation was to improve clinical dosimetry strategies by investigating the impact of temporal sampling, in particular of a late SPECT/CT measurement and dosimetry based on a single SPECT/CT, and patient motion in combination with measurement times on the absorbed dose estimation of lesions and organs-at-risk.

Materials and Methods

In the first study, a reference model was defined by using all four available SPECT/CT measurements (24 h, 48 h, 72 h and 168 h post-treatment) of prostate cancer patients receiving [^{177}Lu]Lu-PSMA-I&T. The best time activity curve (TAC) fit model was evaluated based on common goodness-of-fit parameters. The biologically effective dose (BED) of lesions and kidneys was determined using reduced sampling schedules with three and two time points and compared to the reference. Special focus was on combinations with or without a late SPECT/CT at 168 h post injection, which is usually based on out-patient visits and particularly challenging to realize. In the second study, different methods for STP dosimetry were investigated for all compartments of interest with respect to the best measurement time point and STP dosimetry method depending on the different possible reference protocols. The resulting absorbed doses were compared to the respective reference values. The third study investigated the effect of patient motion during post-therapeutic ^{177}Lu-PSMA-SPECT/CT scans on the absorbed dose estimation. A key aspect of the study was to evaluate the influence of different step times (5 s vs. 15 s per projection) on the dosimetric results. Short step times increase image noise but offer greater for the patient. For this purpose, SPECT projections of a patient-like phantom were simulated in baseline and different shifted positions. By stacking the projections according to randomly selected motion patterns, motion of up to 4 cm was introduced at intervals of 1 and 4 minutes on average. Absorbed dose to lesions and kidneys was compared between motion-affected and motion-free data.

Results

For TAC fitting of the reference models, a bi-exponential, population-based model was best suited for submandibular glands, while no statistically superior model was identified for kidneys and lesions. However, BED deviations between possible reference models reached -19 % for kidneys and -44 % for lesions. The study suggested that late SPECT/CT imaging at 168 h can be omitted for kidneys (0 ± 1 % deviation) and lesions (8 ± 13 % deviation). BED deviations were higher for lesion, but outliers were predictable based on the lesion effective half-life (Pearson correlation coefficient: r = 0.88). Single time point dosimetry was feasible, with deviations of 4 ± 4 % (kidneys), 10 ± 13 % (lesions), and 10 ± 14 % (glands) at 48 h post-treatment using a bi-exponential population-based method. However, absorbed dose deviations, the best STP method and the optimal imaging time point depended on the reference model. To reduce motion effects, the shorter step time of 5 s per projection would be recommended. Nevertheless, absorbed dose deviations reached up to -28 % for lesions and -19 % for kidneys for motion events on average every minute.

Conclusion

Clinical dosimetry with fewer imaging time points and reduced measurement times is feasible by incorporating uncertainty estimates and standardizing reference models. Reducing conventional SPECT/CT acquisition times is advantageous to minimize motion-induced errors and is an alternative to increase patient throughput without reducing the number of SPECT/CT scans during hospitalization. This may facilitate the establishment of routine dosimetry and support personalized therapies.

Zusammenfassung

Zielsetzung

Die SPECT-basierte Dosimetrie für die ^{177}Lu-PSMA-Radioligandentherapie bei Patienten mit metastasiertem Prostatakarzinom, ist nicht nur notwendig, um die absorbierte Dosis in Risikoorganen wie Nieren oder Speicheldrüsen zu überwachen, sondern auch essenziell um Fortschritte in der Etablierung und dem Verständnis von Dosis-Wirkungs-Beziehungen zu erzielen und den Weg zu personalisierten Radionuklidtherapien zu ebnen. Der hohe klinische Arbeitsaufwand, Kosten und die Belastung für die Patienten durch die große Anzahl an SPECT-Scans erschweren jedoch die Etablierung einer routinemäßigen klinischen Dosimetrie. Darüber hinaus ist die SPECT-basierte Dosimetrie aufgrund von Unsicherheiten bei der bild-basierten Aktivitätsquantifizierung fehleranfällig. Da Prostatakrebspatienten häufig unter starken Knochenschmerzen leiden, sind unregelmäßige Patientenbewegungen während der langen Scanzeiten ein wichtiges Thema in der SPECT-Quantifizierung, wurden aber bisher nicht in der Dosimetrie berücksichtigt. Kürzere Messzeiten erhöhen das Bildrauschen, bieten jedoch einen höheren Patientenkomfort. Ziel dieser Dissertation war es, klinische Dosimetrie-Strategien zu verbessern, indem der Einfluss des zeitlichen Samplings, insbesondere der späten SPECT/CT-Messung und der Dosimetrie basierend auf einem einzelnen SPECT/CT, sowie der Patientenbewegungen in Kombination mit Messzeiten auf die absorbierte Dosis von Läsionen und Risikoorganen untersucht wurden.

Material und Methoden

In der ersten Studie wurde ein Referenzmodell definiert, indem alle vier verfügbaren SPECT/CT-Messungen (24 h, 48 h, 72 h und 168 h nach der Therapie) von Prostata-Karzinom Patienten verwendet wurden, die [^{177}Lu]Lu-PSMA-I&T erhalten haben. Das beste Fitmodell für die Zeit-Aktivitäts-Kurve wurde anhand gängiger Anpassungsgüteparameter evaluiert. Die biologisch effektive Dosis (BED) von Läsionen und Nieren wurde mit reduzierten Messprotokollen (drei bzw. zwei Zeitpunkte) berechnet und mit der Referenz verglichen. Besonderer Fokus lag auf Kombinationen mit und ohne einer späten SPECT/CT Messung, 168 h nach der Injektion. Dieses SPECT/CT wird in der Regel ambulant gemacht und die Umsetzung ist besonders herausfordernd. In der zweiten Studie wurden für alle interessanten Kompartimente verschiedene Einzelzeitpunktdosimetriemethoden hinsichtlich des optimalen Messzeitpunkts und der geeignetsten Methode in Abhängigkeit von unterschiedlichen Referenzprotokollen untersucht. Die resultierenden absorbierten Dosen wurden mit den jeweiligen Referenzwerten verglichen. Die dritte Studie untersucht den Einfluss von Patientenbewegungen während posttherapeutischer ^{177}Lu-PSMA-SPECT/CT-Scans auf die Abschätzung der absorbierten Dosis. Ein wichtiger Aspekt der Studie war die Bewertung des Einflusses unterschiedlicher Akquisitionszeiten (5 s versus 15 s pro Projektion) auf die dosimetrischen Ergebnisse. Dafür wurden SPECT-Projektionen eines patientenähnlichen Phantoms in mehreren Positionen simuliert. Durch das Zusammenstecken der Projektionen gemäß zufälliger Bewegungsmuster wurde eine Phantombewegung von bis zu 4 cm in Intervallen von 1 min und 4 min im Mittel eingeführt. Die absorbierte Dosis von Läsionen und Nieren wurde zwischen Datensätzen mit und ohne Bewegung verglichen.

Ergebnisse

Für die Anpassung der Zeitaktivitätskurven-Referenzmodelle erwies sich ein bi-exponentielles, populationsbasiertes Modell als am besten geeignet für die submandibulären Drüsen, während für Nieren und Läsionen kein statistisch überlegenes Modell identifiziert wurde. Die Abweichungen der BED betrugen jedoch bis zu -19 % für Nieren und -44 % für Läsionen. Die Studie legt nahe, dass die späte SPECT/CT-Bildgebung nach 168 Stunden für Nieren (0 ± 1 % Abweichung) und Läsionen (8 ± 13 % Abweichung) weggelassen werden kann. Die Abweichungen der BED waren höher für die Läsionen, wobei Ausreißer anhand von Abweichungen der Läsions-Halbwertszeit vorhergesagt werden konnten (Pearson Korrelationskoeffizient: r = 0,88). Die Einzelzeitpunktdosimetrie war ebenfalls realisierbar, wobei eine Messung 48 h nach der Therapie basierend auf der bi-exponentiellen populationsbasierten Methode zu Abweichungen von 4 ± 4 % (Nieren), 10 ± 13 % (Läsionen) und 10 ± 14 % (Speicheldrüsen) führte. Allerdings hingen die Abweichungen, die optimale Einzelzeitpunktmethode und der beste Messzeitpunkt vom Referenzmodell ab. Zur Reduktion von Bewegungseffekten wird eine kürzere Messzeit von 5 s pro Projektion empfohlen. Dennoch wurden Dosisabweichungen von bis zu -28 % für Läsionen und -19 % für Nieren bei Bewegungen im Mittel jede Minute beobachtet.

Schlussfolgerung

Eine klinische Dosimetrie mit reduzierter Anzahl an Messzeitpunkten und verkürzten Akquisitionszeiten ist durch die Einbeziehung von Unsicherheiten und der Standardisierung von Referenzmodellen möglich. Eine Verkürzung der herkömmlichen SPECT/CT-Aufnahmezeiten ist vorteilhaft, um bewegungsbedingte Fehler zu minimieren, und stellt eine Alternative dar, um den Patientendurchsatz zu erhöhen, ohne die Anzahl der SPECT/CT-Scans während des Krankenhausaufenthalts zu verringern. Dies kann die Implementierung einer routinemäßigen Dosimetrie erleichtern und personalisierte Therapien unterstützen.

1 Background

This chapter provides the foundational background necessary to understand the principles of dosimetry in ^{177}Lu-PSMA therapy. It includes an overview of the therapy itself, the fundamentals of SPECT imaging and quantification, and key concepts of dosimetry.

1.1 Overview of ^{177}Lu-PSMA Therapy

Prostate cancer is the second most commonly diagnosed cancer worldwide with an estimated 1.46 million new cases in 2022. While the mortality rate has decreased by 0.8 %, the number of new cases is likely to increase in the next decades due to demographic changes and growing global population [1, 2]. ^{177}Lu-PSMA therapy represents a targeted radionuclide treatment with promising results in prostate cancer patients, e.g. a prolonged progression-free survival [3]. The radioligand selectively binds to tumor-associated receptors, in this case the prostate-specific membrane antigen (PSMA), which is overexpressed in metastatic castration-resistant prostate cancer (mCRPC) [4]. The therapeutic molecule consists of a pharmacophore, which is a glutamate-urea-lysine motif that selectively targets PSMA on prostate cancer cells. The linker binds this pharmacophore to the chelator (DOTA), which in turn carries the radionuclide, $^{177}_{71}$Lu [5]. ^{177}Lu undergoes β^--decay with a physical half-life of 6.65 days, transforming into stable $^{177}_{72}$Hf. The emitted β^--particles, with a maximum energy of 497 keV and a maximum soft tissue penetration range of 1.7 mm, are ideal for treating small tumors, whereas the accompanying γ-emissions with energies of 113 keV and 208 keV (abundances of 6.2 % and 10.4 %, respectively) are suitable for gamma camera imaging [6, 7].

Currently, two radiopharmaceuticals are available for ^{177}Lu-PSMA therapy: [^{177}Lu]Lu-PSMA-I&T and [^{177}Lu]Lu-vipivotide tetraxetan (Pluvicto®; Novartis), formerly known as [^{177}Lu]Lu-PSMA-617. The development of [^{177}Lu]Lu-PSMA-617 began in 2012 with initial diagnostic and therapeutic applications reported in 2014. Following multi-center studies and the phase III VISION trial, [^{177}Lu]Lu-PSMA-617 (Pluvicto®) received approval by the FDA in March 2022 as the first PSMA-targeting therapeutical compound [8]. European Medicines Agency (EMA) approval followed in December 2022 [9]. In the VISION trial, patients were selected based on PSMA-positive imaging, i.e. PSMA-positive ^{68}Ga–labeled PSMA-11 positron-emission computed tomography/computed tomograpy (PET/CT) scans and were randomly assigned to receive either [^{177}Lu]Lu-PSMA-617 in combination with standard care or standard care alone [3]. The study found that the addition of [^{177}Lu]Lu-PSMA-617 significantly prolonged both imaging-based progression-free survival (median 8.7 vs. 3.4 months) and overall survival (median 15.3 vs. 11.3 months) compared to standard care alone. Although the incidence of grade 3 or higher adverse events was higher in the [^{177}Lu]Lu-PSMA-617 group (52.7 % vs. 38.0 %), quality of life was not adversely affected [3]. Potential candidates for ^{177}Lu-PSMA therapy are patients with metastatic castration-resistant prostate cancer (mCRPC) who have progressed after standard treatments including androgen deprivation therapy and chemotherapy [3]. For final eligibility for ^{177}Lu-PSMA therapy, the expression of the prostate-specific membrane antigen of the cancer cells must be confirmed, which is usually performed with diagnostic ^{68}Ga- or ^{18}F-PSMA PET imaging [10]. Further pre-treatment assessment includes the evaluation of blood parameters, as well as renal function assessments via scintigraphy [11–13]. Current recommendations suggest a maximum of 6 cycles of ^{177}Lu-PSMA therapy each with a total activity of 7.4 GBq, administered at intervals of 6 ± 1 weeks and intermittent PET-imaging to monitor disease progression [14].

Since PSMA is also expressed in healthy organs such as the kidneys, salivary glands, and small intestine, these organs are considered at risk during ^{177}Lu-PSMA therapy [12, 15]. To monitor activity uptake and absorbed dose in these organs over multiple therapy cycles and avoid radiation-induced toxicity, planar scintigraphy or quantitative single photon emission computed tomography (SPECT) imaging are suggested [14]. However, Rosar et al. demonstrated that two-dimensional planar imaging underestimates the absorbed dose to lesions and organs-at-risk [16]. Consequently, three-dimensional SPECT imaging is recommended, particularly for lesion dosimetry. Figure 1.1 presents an overview of a typical ^{177}Lu-PSMA therapy for an exemplary patient undergoing six cycles, with three ^{18}F-PSMA PET scans performed at baseline, during, and after six cycles of therapy. After each ^{177}Lu-PSMA injection, hybrid SPECT/CT acquisitions are utilized to quantitatively assess radionuclide uptake and determine absorbed doses in organs-at-risk and lesions. In this example, three post-therapeutic scans are conducted at 24, 48, and 72 hours after compound administration.

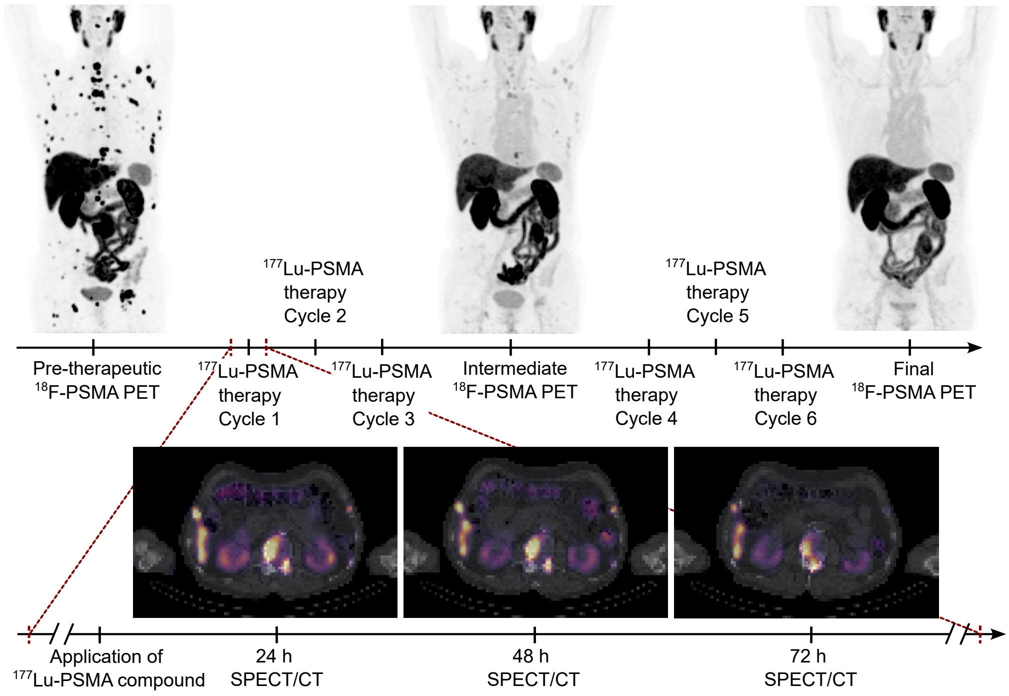

FIGURE 1.1: **Schematic overview of ^{177}Lu-PSMA therapy.** This exemplary patient went through six cycles of ^{177}Lu-PSMA therapy, along with three ^{18}F-PSMA PET acquisitions for baseline, staging and follow-up. Three quantitative SPECT/CTs were acquired at 24 h, 48 h and 72 h after injection of ^{177}Lu-PSMA. One exemplary transverse slice of the SPECT/CT fusion is shown, visualizing uptake in kidneys, intestine and bone lesions.

1.2 SPECT Imaging and Quantification

As outlined in the previous section, sequential quantitative SPECT imaging is the foundation for dosimetry in ^{177}Lu-PSMA therapy. The following sections introduce the fundamental principles of SPECT imaging, including the design and function of the gamma camera for acquiring activity projections, the subsequent image reconstruction and quantification processes, and a brief overview of Monte-Carlo-based simulations used to model SPECT acquisitions.

1.2.1 Gamma Camera

Quantitative SPECT imaging enables to measure the three-dimensional activity distribution of γ-emitting radionuclides in physical units of Becquerel. A hybrid SPECT/CT system comprises two to three detector heads that rotate around the patient, acquiring two-dimensional projections over 360 degrees, followed by a CT scan. Each camera head consists of several layers, which are illustrated schematically in Figure 1.2. The first layer is a collimator made of a material with high density and atomic number (e.g. lead or tungsten), which can be adjusted in thickness depending on the radionuclide-specific photon energy. The collimators usually used for SPECT imaging of ^{177}Lu feature an array of parallel holes separated by septa, allowing only photons from a specific direction to pass through to the adjacent scintillation crystal. Commonly made of a NaI(TI) (thallium-doped sodium iodide) crystal, it absorbs γ-photons and converts them into optical photons [17–19]. Connected via a light guide, a closely packed array of photomultiplier tubes behind the scintillation crystal converts the visible light into a spatially locatable electrical signal [19]. The location of γ-ray interactions is determined by calculating the weighted average of signals from multiple photomultiplier tubes which is referred to as the 'Anger principle' [19]. The photomultiplier tubes convert the photons into an electrical signal which is amplified, read out and post-processed by corresponding electronics generating pixelized projections [20]. Photons interact with matter thoughout the entire detection process, e.g. in the patient, the detector or scintillation crystal and the collimator. These interactions include elastic (coherent) scattering, inelastic (Compton) scattering or absorption by the Photoelectric effect [21]. During elastic scattering, the photon energy is conserved but the photon alters its direction. In Compton scattering, the photon interacts with an outer-shell electron, which is ejected from the atom while the photon is scattered with reduced energy and altered direction. The photoelectric effect occurs when a photon transfers its entire energy to a bound electron in the inner atomic shells, which is ejected as photoelectron. The resulting vacancy is filled by an outer-shell electron which leads to the emission of characteristic X-ray or Auger electrons [21]. All these interactions can degrade the image quality and lead to a loss in photon flux by attenuation or to unwanted scatter in the final image. Figure 1.2 shows some examples of these image degrading effects. Septal penetration can occur, particularly for medium- to high-energy photons [22]. Medium-energy collimators in ^{177}Lu-SPECT imaging have a spatial resolution in the range of 1 to 2 cm [23].

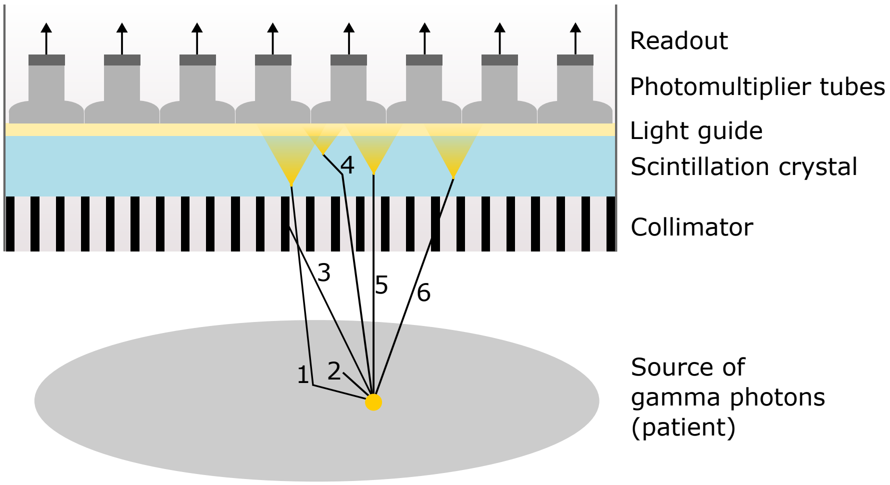

Figure 1.2: **Schematic illustration of a SPECT detector with image degrading effects.** The gamma camera consists of multiple layers, and gamma photons emitted from within the patient can undergo various interactions before reaching the photomultiplier tubes. Photons may be scattered (1) or absorbed within the patient (2), absorbed by the collimator (3), scattered inside the detector (4) or penetrate the collimator septa (6). Only in case (5), the point source is imaged correctly. Adapted from [24] and [25]

1.2.2 Reconstruction

Projection data can be reconstructed using various reconstruction algorithms. Today, the most commonly applied method is ordered-subset expectation maximization (OSEM), which is based on the principle of maximum-likelihood-expectation-maximization (MLEM) described schematically in Figure 1.3. Detailed information on SPECT image reconstruction can be found in [26, 27]. MLEM tries to iteratively improve the image data f by maximizing the likelihood that its forward projection $\hat{p}$ represents the measured projection data p. The process starts with an initial, non-zero guess $f_j^{(0)}$. For each iteration k, the current image estimate $f_j^{(k)}$, i.e. photon counts in voxel j is forward projected to determine the estimated projection data $\hat{p_i}^{(k)}$ in projection pixel i:

$$\hat{p_i} = \sum_l a_{il} f_l^{(k)}. \tag{1.1}$$

The system matrix a_{ij} can be described as the probability that a photon emitted from voxel j is detected in the projection pixel i. The ratio between the measured and estimated projection data is calculated for each projection pixel i and the voxel values are updated by back-projecting the ratio [26]:

$$f_j^{(k+1)} = f_j^{(k)} \cdot \frac{1}{\sum_i a_{ij}} \sum_i \frac{p_i}{\sum_l a_{il} f_l^{(k)}} a_{ij}. \tag{1.2}$$

The ordered-subset expectation maximization (OSEM) algorithm is often preferred, as it updates the image by utilizing only subsets of projection data, hence reducing the number of calculations per update. This results in faster convergence of the reconstruction process and thus a decrease of the overall reconstruction runtime [26, 27]. The OSEM is described by

$$f_j^{(k+1)} = f_j^{(k)} \cdot \frac{1}{\sum_{i \in S_n} a_{ij}} \sum_{i \in S_n} \frac{p_i}{\sum_l a_{il} f_l^{(k)}} a_{ij}, \tag{1.3}$$

where S_n describes the n^{th} subset [27]. The algorithms converges towards the maximum likelihood solution with increasing number of iterations. However, perfect agreement of the measured and calculated projections is not possible due to inherent Poisson noise. The MLEM algorithm tends to carry the noise into the reconstructions with increasing number of iterations, since it converges at different rates for different spatial frequencies: low frequencies converge faster than high ones due to the smoothing (low-pass) effect of back projection [26]. Consequently, limiting the number of iterations or incorporating regularization is necessary, e.g. by limiting the differences between neighboring voxels through quadratic penalties. Therefore, equation 1.3 changes to

$$f_j^{(k+1)} = f_j^{(k)} \cdot \frac{1}{\sum_{i \in S_n} a_{ij} + \beta \left(\frac{f_j^{(k)} - A_j}{A_j} \right)} \sum_{i \in S_n} \frac{a_{ij}}{\sum_l a_{il} f_j^{(k)}} p_i, \tag{1.4}$$

where $A_j = \sum_{l \in N_j} w_{jl} f_l^{(k)}$, β is the Bayesian weight, N_j is the neighborhood of voxel j and w_{jl} is the prior weight (i.e. inverse of the distance from the central voxel) [27]. Including prior information is referred to as maximum-a-posteriori (MAP) reconstruction [28].

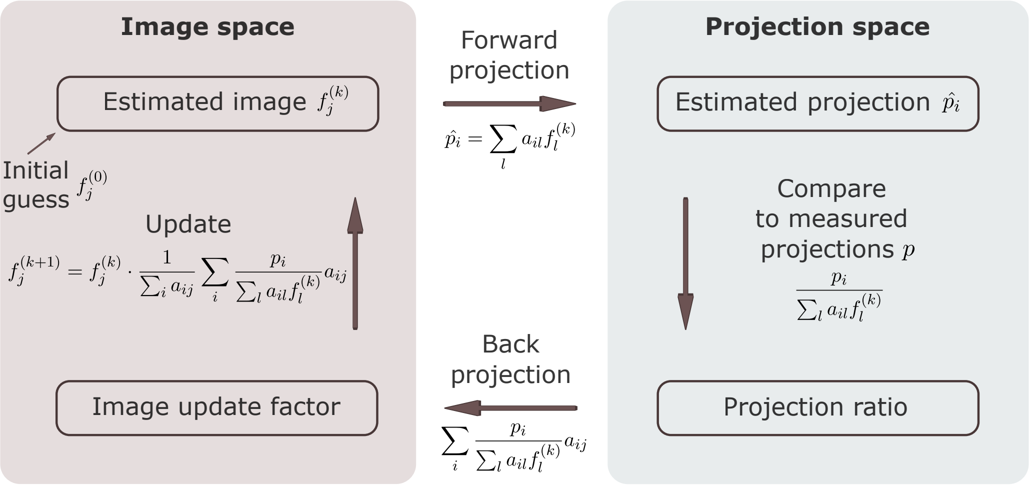

FIGURE 1.3: **Schematic of the MLEM algorithm.** The reconstruction image in image space is estimated iteratively by minimizing the error between the estimated and measured projections in the projection space. Figure adapted from [29].

1.2.3 Quantification

For correct activity quantification, several physical effects that distort the measurement process have to be corrected for. The most commonly applied corrections include those for attenuation, scatter and collimator-detector-response. Attenuation correction is performed using the distribution of attenuation coefficients obtained from the CT scan. To compensate for scatter in the patient, collimator, crystal or any other part of the camera (see Figure 1.2), model- or measurement-based algorithms are available. In model based scatter correction, scatter projections are estimated by forward projection of scattered photons using the so-far reconstructed image and the density map derived from the CT. In measurement-based scatter correction, multiple energy windows are acquired adjacent to the photopeak to estimate the scatter projection. For the upper photo-peak of ^{177}Lu at 208 keV, a triple energy window approach is usually used as illustrated in Figure 1.4. Scatter windows are acquired at energies below and above the photo-peak to estimate the proportion of scattered photons within the emission window with a trapezoidal approximation (purple area in Figure 1.4). The third correction that is usually employed is the compensation for the collimator-detector-response, which describes how a point source is imaged by the system depending on the source-to-collimator distance. For ^{177}Lu, the energy of the emitted photons is low enough so that approximately 90 % of the detected photons within the energy window around the photo-peak are allowed by the collimator geometry, i.e. are not scattered in the collimator or penetrate the septa. Thus, a Gaussian function with distance-dependent full-width-half-maximum (neglecting collimator scatter and penetration) is a good approximation for the absorption spectrum of ^{177}Lu [22].

For the final quantification step of SPECT imaging, calibration is essential to convert photon counts per voxel, f_j, to activity concentration, C in [Bq/ml]. For this, a measurement of a sufficiently large and homogeneously filled phantom with known

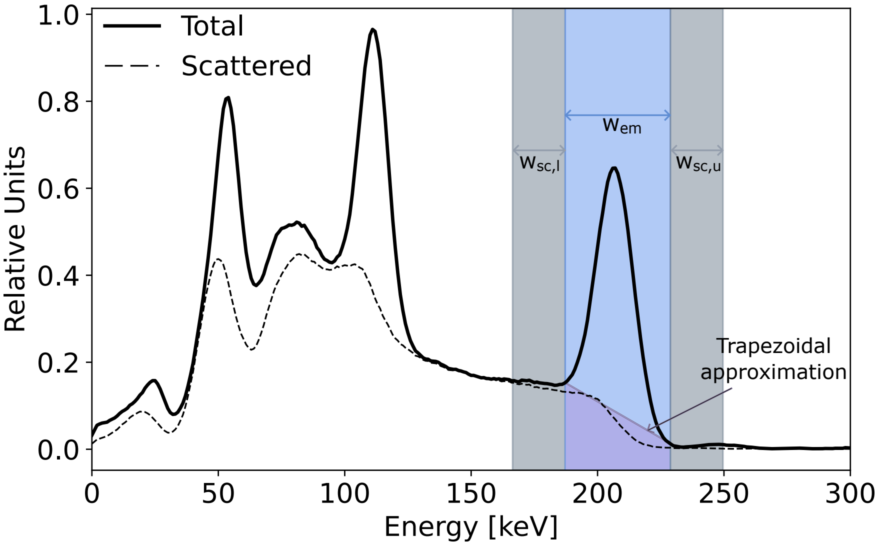

FIGURE 1.4: **Energy spectrum for a ^{177}Lu-SPECT simulation.** The energy spectrum including the total and scattered events for a ^{177}Lu SPECT-simulation of a patient phantom is plotted with the emission window w_{em} at the 208 keV peak and the adjacent lower ($w_{sc,l}$) and upper (w_{sc_u}) scatter windows. One approach for estimating the amount of scatter in the emission window is the trapezoidal approach (area in purple).

activity concentration (C_{true}) of the respective nuclide should be acquired, using the same parameters as for the patient measurements. The calibration factor CF is then given by: [30]:

$$CF = \frac{C_{true}}{f_j} \cdot t \cdot V \tag{1.5}$$

with the acquisition time per projection t and the voxel volume V.

Despite the aforementioned corrections, SPECT/CT imaging remains subject to various sources of uncertainty [31]. For instance, the limited resolution of SPECT imaging leads to spill-over of activity into the background or spill-in of background activity into the object. This partial volume effect particularly impacts the accurate quantification of activity in small objects near the resolution limit of the system [22]. One method to assess and correct for this effect involves the use of recovery coefficients (RCs), defined as the ratio of the measured activity concentration to the true activity concentration [32]. RCs are typically determined using phantoms with spheres of known sizes and activities—such as the NEMA IEC body phantom—acquired under the same imaging conditions as patient scans. However, recent studies found that RCs depend on the object-to-background ratio of the measurement, the shape of the object and the positioning of the objects inside the phantom [23, 33]. Therefore using them as a tool to correct for spillover can be challenging. More advanced methods, like the iterative Yang partial volume correction (PVC) use segmentation masks and the three-dimensional point spread function of the imaging system to correct iteratively for the system resolution [34, 35]. Recent developments also include deep-learning in PVC as investigated by Leube et al. [36]. The U-Nets were trained with simulations of 10000 random activity distributions and showed a superior performance to SPECT without partial volume correction and with iterative Yang PVC. Alternatively, enlarged volumes-of-interest (VOIs) could be used for the determination of the activity concentration to account for spill-over counts [37]. Other corrections, such as those for dead time and motion, are less frequently used in SPECT. Particularly motion correction remains a topic of ongoing research.

1.2.4 Monte-Carlo-based SPECT Simulation

To further investigate and improve imaging systems, corrections and reconstruction techniques in nuclear medicine, Monte Carlo simulations can be used. Monte-Carlo simulations are particularly well suited to model stochastic processes such as radioactive decay and photon interactions with matter. They rely on random sampling from probability distributions that describe physical processes like photon emission, absorption and scattering. In the context of SPECT imaging, one widely used and well-established Monte-Carlo simulation tool is the Fortran-90-based software SIMIND [38]. Detailed information on Monte-Carlo simulation pipeline and methods used in SIMIND can be found in [39]. SIMIND allows the user to define a voxel-based source map that describes the spatial activity distribution within a phantom using integer values to represent relative activities. For each decay event, the source location is sampled uniformly from this map, and a photon is emitted with an energy drawn from the radionuclide's decay scheme. To improve simulation efficiency without compromising statistical accuracy, the direction of photon emission is sampled within a forced direction toward the detector, which is an example of a variance reduction technique. The probability for the photon to travel a certain distance in a material is defined by the Beer-Lambert law. This includes the linear attenuation coefficient depending on the photon energy and atomic number of the material, which can be defined by the density map in SIMIND. After traveling a sampled path length, the photon may undergo one of several interaction processes with matter: Photoelectric absorption, Compton scattering, or coherent scattering and pair production (at energies ≥ 1.02 MeV). The type of interaction depends on random sampling from probability distributions defined by the respective cross-sections. If a photon reaches the detector, SIMIND continues to simulate its interactions with the gamma camera components, including the collimator, the crystal and the protection cover [39].

1.3 Dosimetry

This thesis focuses on image-based dosimetry in ^{177}Lu-PSMA therapy. The following sections explain the general motivation behind performing dosimetry, how multiple quantitative SPECT/CT acquisitions are used to calculate the absorbed dose to various tissues, and how biological effects can be incorporated into the dosimetric evaluation.

1.3.1 Motivation

The determination of absorbed doses in lesions and organs-at-risk following ^{177}Lu-PSMA therapy is essential for multiple reasons. In European member states, this is a legal requirement under the European Basic Safety Standards Directive (Council Directive 2013/59/Euratom, Article 56), which mandates individual absorbed dose and dosage assessments for all therapeutic procedures involving ionizing radiation [40]. Despite this directive, patients currently receive a standardized administered activity of 7.4 GBq per cycle, which corresponds more to a pharmaceutical approach rather than a radiotherapy approach driven by patient-specific dosimetry. Standardized dosing may not be optimal for all patients, as demonstrated in Figure 1.5, which presents two patients with different total tumor volumes. Patient A, with a smaller total tumor burden (16 ml), received a renal absorbed dose of 2.2 Gy, while Patient B, with a substantially larger total tumor volume (417 ml), received only 1.2 Gy. This inverse relationship reflects the tumor-sink-effect, where high tumor load reduces physiological uptake in normal organs [41]. These findings suggest that Patient A could have tolerated, and potentially benefited from, a higher administered activity. However, in patients with extensive tumor load, increased radiopharmaceutical uptake may also result in elevated absorbed doses to non-target tissues such as the bone marrow, increasing the risk of hematological toxicity. Additionally, the renal absorbed dose is influenced by other patient-specific factors such as renal function, perfusion, and underlying comorbidities, which must be carefully considered in individualized treatment planning.

However, for enabling personalized treatment, routine implementation of dosimetry is essential. Accumulating more patient-specific dosimetric data is necessary to generate robust evidence to which extent individualized dosing affects both, treatment efficacy and safety. While dose-response relationships have been extensively studied in patients undergoing ^{177}Lu-DOTA-TATE therapy for metastatic neuroendocrine tumors, such correlations remain less well-defined in ^{177}Lu-PSMA therapy. A study by Sejin Ha et al. investigated tumor response in 20 patients receiving ^{177}Lu-DOTA-TATE therapy, with single time point (STP) SPECT/CT imaging performed four to five days post-injection (p.i.) [42]. Target lesions, identified based on the highest uptake in SPECT with a diameter > 10 mm, were monitored for anatomical changes before and after therapy, and their standardized uptake value (SUV $=$ activity concentration $\cdot$ patient weight/injected activity) and absorbed dose estimates were determined. The study demonstrated a significant correlation between cumulative tumor absorbed dose and the percentage reduction in lesion diameter, and it proposed potential absorbed dose thresholds predictive of treatment response [42]. Similarly, a prospective observational study by Garske-Román et al. involving 200 patients treated with ^{177}Lu-DOTA-octreotate found that a higher number of treatment cycles was associated with improved overall survival [43]. This benefit was observed in patients who were able to complete therapy cycles until reaching a cumulative renal absorbed dose of 23 Gy, defined as the maximum tolerable dose to the kidneys [43]. Further, a sub-study of the VISION trial involving 30 patients receiving [^{177}Lu]Lu-PSMA-617 therapy found a mean cumulative renal absorbed dose of only 15.0 ± 5.8 Gy after six cycles, well below the 23 Gy threshold [44]. These findings suggest that, in certain cases, exceeding the standard six therapy cycles may be feasible without exceeding renal dose limits. It is important to note that current absorbed dose thresholds in radioligand therapy are based on experience from external beam radiation therapy, which are not necessarily directly applicable due to differences in dose rates and biological effectiveness [45, 46]. This highlights the need for routine dosimetry in a large patient cohort to refine absorbed dose thresholds, optimize treatment efficacy, and improve patient outcomes.

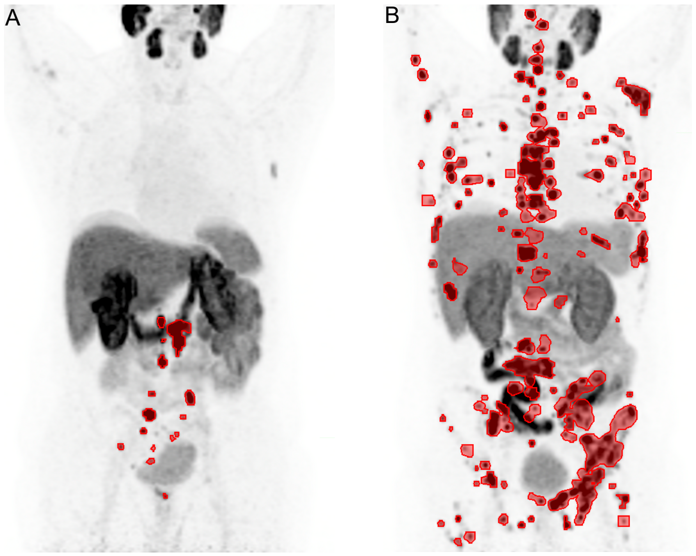

Total tumor volume	16 ml	417 ml
Mean renal absorbed dose	2.2 Gy	1.2 Gy

FIGURE 1.5: **Motivation for personalized dosimetry.** The two exemplary patients shown in this figure both got administered an injected activity of 7.4 GBq Pluvicto®. The total tumor burden is highlighted in red. Patient B has a higher total tumor volume of 417 ml than patient A with 16 ml but a lower renal absorbed dose of 1.2 Gy (versus 2.2 Gy in patient A) which indicates that patient B potentially could have benefited from a higher therapeutic activity.

1.3.2 Absorbed Dose Calculation

The absorbed dose D of a specific target region (organs, tumors or single voxels) caused by radioactive decays in a source region can be estimated using the Medical Internal Radiation Dose (MIRD) formalism

$$D_{target} = TIA_{source} \cdot S_{source \rightarrow target} \text{ with } S_{source \rightarrow target} = \frac{\Delta \cdot \varphi_{source \rightarrow target}}{m_{target}}, \tag{1.6}$$

with the time integrated activity (TIA) corresponding to the total number of decays, and the S-value (S). The S-value describes the mean absorbed dose deposition per radioactive decay, and is calculated by the mean emitted energy Δ per decay, times the fraction of energy deposited in the target region φ, divided by the target mass m [18]. S-values are tabulated (e.g. OLINDA or OpenDose [47, 48]) for many source-to-target combinations, radionuclides, and human or animal reference geometries, i.e. phantoms, including standardized target masses. Therefore, S-values have to be corrected for the patient-specific target mass, i.e. in case of electron dose via [47, 48]:

$$S_{patient} = S_{phantom} \cdot \frac{m_{phantom}}{\rho_{patient}\ V_{patient}}. \tag{1.7}$$

In the case of ^{177}Lu decay, the β^--particle range in soft tissue is maximally 1.7 mm, which justifies the approximation that the absorbed dose to the target region is equal to the self-absorbed dose (source equal to target region) in all regions with a significant uptake of the radiopharmaceutical. For the calculation of the TIA, the time-activity-curve (TAC) in the respective source region has to be monitored to map the pharmacokinetics of the radiopharmaceutical. This can be done via multiple quantitative SPECT acquisitions measuring the distribution of the activity concentration in the patient at different time points after therapy. The activity concentrations in different target VOIs can then be fitted to a suitable function best describing the pharmacokinetics of the radiopharmaceutical [16, 49–51]. In the simplest case of only one pharmacokinetic phase, a mono-exponential model can be used:

$$A(t) = A_0 \cdot \exp\left(-\frac{\ln(2)}{T_{1/2,eff}} \cdot t\right), \tag{1.8}$$

with the effective half-life $T_{1/2,eff}$ being a combination of the physical and the biological half-life:

$$T_{1/2,eff} = \frac{T_{1/2,phys} \cdot T_{1/2,bio}}{T_{1/2,phys} + T_{1/2,bio}}. \tag{1.9}$$

If there are multiple pharmacokinetic phases, the TAC can be described by a sum of exponential functions. Ideally, more data points than free fitting parameters should be available, which requires at least three activity measurements per pharmacokinetic phase with two free parameters [51]. For [^{177}Lu]Lu-PSMA-617, the maximum concentration of labeled PSMA in a solid tumor is reached around 33 h after administration, where the maximum concentration of the membrane-bound drug is reached earlier than the maximum of the internalized drug (approximately 17 h versus 48 h p.i.) [52]. Peak plasma concentration is reached earlier, at around 20 min after administration [44].

While collecting more data points would improve the methodological accuracy, it leads to logistical challenges in the clinical practice due to a high workload, limited scanner capacity and significant patient burden. Approximating the absorbed dose using a single SPECT/CT measurement is gaining popularity. On the one hand, STP dosimetry offers advantages such as reduced clinical workload, more efficient logistics (e.g. no need for outpatient scans) and improved patient comfort. On the other hand, it introduces greater uncertainties in the calculated absorbed dose values. Therefore, it is essential to define a reliable reference to assess the errors associated with different STP dosimetry methods and measurement time points [53]. Several methods exist to approximate the TIA from a single measurement, typically relying on assumptions about the radionuclide's pharmacokinetics in the respective target organ or tumor [54, 55]. For instance, a straightforward approach to estimate the TIA$_{\mathrm{STP}}$ assuming a mono-exponential decay is given by the following equation:

$$\mathrm{TIA}_{\mathrm{STP}} = \frac{T_{1/2,eff}}{\ln(2)} \frac{A(t_{SPECT})}{\exp(-(\ln(2)/T_{1/2,eff}) \cdot t_{SPECT})}. \tag{1.10}$$

Here, $A(t_{SPECT})$ is the activity concentration in the target region measured at time t_{SPECT}. The effective half-life $T_{1/2,eff}$ is fixed in this approximation and can be derived e.g. from data of a similar patient population or previous therapy cycles of the same patient.

1.3.3 Biological Dose Concepts

The absorbed dose describes the physical quantity of energy deposited by ionizing radiation per unit mass of tissue. However, especially in medical applications, it is also important to consider the biological response of tissues and cells to radiation. This has lead to the development of biological dose concepts which aim to represent radiation-induced biological damage more accurately.

In the decay of ^{177}Lu, high energy γ-photons and electrons are emitted. In general, the high energy γ-photons do not ionize atoms directly but interact with matter primarily through the Photoelectric effect and Compton scattering, as explained earlier (see Section 1.2). Ionization along the particle tracks is caused by secondary electrons generated by these interactions and by primary electrons emitted during the β^--decay of ^{177}Lu. They either result in direct DNA damage (e.g. strand breaks) (Figure 1.6 **a**) or indirect damage through the generation of reactive oxygen species, particularly hydroxyl radicals (OH·), hydrogen peroxide (H_2O_2), and superoxide (O_2·−) (Figure 1.6 **b**) [56]. Since biological tissues are composed of approximately 70 % water, indirect damage is particularly relevant. DNA damage includes single-strand breaks (SSB), double-strand breaks (DSB), base modifications, and DNA-protein or DNA-DNA crosslinking. Cells possess various repair mechanisms to counteract such damage (c.f. Figure 1.6 **c**). These mechanisms may either successfully repair the damage, induce cell death through apoptosis or mitotic catastrophe, or lead the cell into a state of senescence [56]. Improper repair can result in mutagenesis, altering the genetic information of a cell. The cellular response to radiation depends on the radiation type and dose, the dose rate, the cell cycle phase and the cell type with its corresponding repair capacity [57]. The probability of successful repair is lower for DSBs [21, 58].

Several radio-biological concepts have been developed to quantify these effects. One key concept is the relative biological effectiveness (RBE), which compares the biological impact of any type of ionizing radiation to a reference radiation, based on the ability to produce the same biological effect (e.g. cell death or DNA damage) [59]. The linear energy transfer (LET) describes the energy deposition per unit path length. High LET radiation, e.g. α-particles or heavy ions, deposits a large amount of energy in a short distance leading to clustered DNA damage (e.g. DSBs), which is more difficult for the cell to repair. In contrast, low LET radiation, like X-rays, γ-rays or β-particles, mostly cause SSBs, which are more likely to be successfully repaired. As LET increases, the RBE generally increases as well - up to a point beyond which further increases in LET do not produce proportionally greater biological damage, as the cells are already lethally damaged [21, 60]. The biologically effective dose (BED) is a well-established concept in radioligand therapy and is used throughout this thesis. To understand BED, the linear-quadratic (LQ) model must be introduced, which describes cell survival as a function of absorbed dose. Detailed information on both principles can be found in [61, 62]. The LQ model accounts for two different kind of damage that lead to cell death: First, type-A damage occurs when a single ionization event is sufficient to cause lethal DNA damage, such as an irreparable DSB. This represents the intrinsic radio-sensitivity of the tissue. Second, type-B damage results from the accumulation of two sublethal ionizing events within

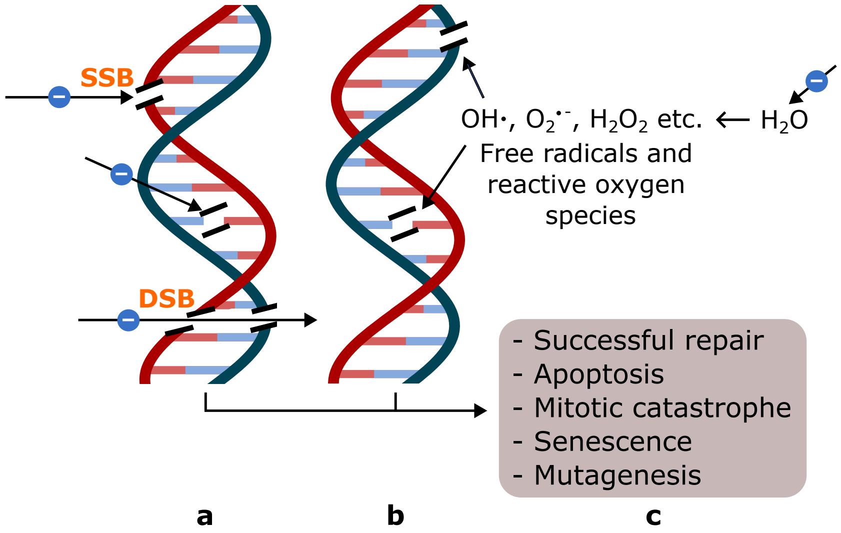

FIGURE 1.6: **Effects of ionizing radiation.** The primary or secondary electrons from the radioactive decay can either directly damage the DNA in cells through SSBs, DSBs or base modifications (**a**) or indirectly damage the DNA through the production of free radicals and reactive oxygen species (**b**). Cells react with various repair mechanisms leading to different outcomes (**c**). Figure adapted from [21] and [58].

one cell. If the second event occurs before repair of the first is complete, the combination can be lethal. Thus, the probability of cell death depends on the cell's repair half-life and the dose rate. The linear quadratic model describes the cell survival S as a function of absorbed dose D and includes these two types of events (type-A and type-B damage):

$$S = \exp(-(\alpha D - \beta D^2)), \tag{1.11}$$

where the linear term αD describes the type-A, single-hit events. The quadratic term βD^2 accounts for type-B damage. Since lethal damage depends on the probability of two independent events, they are proportional to the square of the dose. When the linear component dominates, tissues are considered early-responding, and total dose is more important than how it is fractionated. When the quadratic component dominates (late-responding tissues), the dose per session is more critical, and fractionation can help spare healthy tissue. Tissues with a high α/β-ratio (e.g. some tumors and skin) respond early, while tissues with a low ratio (spinal cord, kidneys, brain) respond late [61, 62]. This concept was originally developed for external beam radiation therapy, where treatments are typically delivered in multiple smaller fractions over several sessions. This allows healthy tissue to repair sublethal damage between treatments, while tumors - which often have less efficient repair mechanisms - accumulate lethal damage. Thus, the concept of BED enables optimization of fractionation schemes and dosing to maximize tumor control and minimize toxicity. The BED concept was adapted to radioligand therapy, where the dose rate depends on the physical and biological half-life of the radionuclide [63]. BED in this context is calculated using the tissue-specific α/β-ratio and the following formula:

$$BED = D \cdot \left(1 + \frac{D}{\alpha/\beta} \cdot G\right) \tag{1.12}$$

where D again is the absorbed dose, and G is the Lea-Catcheside factor. This factor includes the effective clearance rate λ_{eff} and the repair rate of the tissue μ:

$$G = \frac{\lambda_{eff}}{\mu + \lambda_{eff}} \tag{1.13}$$

in the case of mono-exponential clearance [63, 64].

2 | Studies

In the following chapter, the key challenges in image-based ^{177}Lu-PSMA dosimetry are presented. Three studies conducted as part of this dissertation specifically address these challenges, and their main findings are briefly summarized [65, 66].

2.1 Challenges in ^{177}Lu-PSMA Dosimetry

The primary goal of radioligand therapy is to deliver a sufficient absorbed dose to tumor tissue while minimizing toxicity to organs-at-risk [67]. However, clear dose-response relationships to define a 'sufficient' absorbed dose have not yet been established. Further, organ toxicity is monitored via clinical parameters rather than predictive absorbed dose thresholds [14]. Long-term toxicity data for critical organs like kidneys and bone marrow remain insufficient, making it difficult to establish dose limits [68]. In principle, routine post-therapeutic planar or SPECT/CT imaging after ^{177}Lu-PSMA therapy is well established in clinical practice [51]. Nevertheless and despite its potential benefits, image-based dosimetry has not yet been fully integrated into routine clinical workflows due to several challenges that will be discussed in the following.

Reliable dosimetry requires a sufficient number of activity measurements to accurately sample the TAC. This leads not only to a high patient burden, but also poses challenges to the clinical infrastructure due to high device usage and a financial burden due to a potential lack of reimbursement. This is exacerbated by previous EMA and FDA approvals of Pluvicto® and its more recent extended indication for use prior to chemotherapy by the FDA, both of which will lead to a sharp increase in treated patients [69].

Additionally, in most countries, patients are discharged from the hospital shortly after therapy or within 24 h after therapy, requiring SPECT scans to be performed on outpatient basis. This can be inconvenient or unfeasible, especially for patients who live far from the hospital. In Germany, where patients are typically discharged 48 h to 72 h after therapy, early imaging can be performed during hospitalization, but later scans are often difficult or impossible to realize [70]. Meanwhile, current guidelines recommend late imaging three to seven days after therapy, especially for lesion dosimetry [30, 51]. However, the real quantitative impact of omitting a late SPECT/CT measurement on patient dosimetry remains unclear.

Another practical approach to address some of the challenges including patient burden, high device usage and costs mentioned above is to perform dosimetry based on only one SPECT/CT measurement (STP dosimetry). Table 2.1 provides an overview of studies on STP dosimetry in ^{177}Lu-PSMA therapy from recent years. The different studies have attempted to optimize or compare different STP dosimetry methods with multi-time-point reference protocols varying in number and timing of acquisitions and TAC fitting models. As a result, the optimal imaging time points for STP dosimetry of both lesions and organs-at-risk vary between studies and no clear recommendation can be made. Reducing the number of measurement time points to a single acquisition increases the error in absorbed dose estimates and may introduce a systematic bias that should be considered. However, it remains difficult to quantify this bias. Multi-time-point based dosimetry itself, which is used as a reference, is associated with high uncertainties and lacks standardization. Peters et al. report errors of 15 % for kidneys and 14 % for lesions with five-time-point SPECT/CT-based dosimetry [71]. The true pharmacokinetics remain unknown due to limited TAC sampling and may also vary between patients or treatment cycles [72]. Tumor heterogeneity, variations in blood flow, and dynamic changes in receptor expression lead to patient-specific differences in tracer uptake and clearance, making it difficult to standardize dosimetric approaches and corresponding fit models.

Another logistical constraint is the long acquisition time of SPECT. Even with short acquisition protocols of 5 s per projection, SPECT/CT scans typically require at least 5 min per bed position. In many departments, the standard acquisition time is still at least 15 s per projection, resulting in a total scan time of 15 minutes per bed position [51, 71, 73, 74]. To cover the most important organs, two to three bed positions are required, further increasing the scan time to more than 45 minutes. These long scan times result in limited imaging resources, increased patient discomfort or pain, and an increased likelihood of patient movement during scans. Especially patients with advanced prostate cancer often suffer from severe pain due to a high skeletal tumor burden, making abrupt movements more likely [75]. This can lead to artifacts (e.g. blurring of the activity distribution), misalignment between SPECT and CT images, and introduce a significant source of uncertainty in the already challenging dosimetry of lesions and organs-at-risk [76]. Supporting this, previous studies have demonstrated that motion can significantly affect diagnostic and dosimetric accuracy in other SPECT applications. They have shown that motion in myocardial perfusion SPECT increases false-positive rates for coronary artery disease, and respiratory motion in liver SPECT for selective internal radiation therapy (SIRT) significantly increases uncertainties in absorbed dose calculation [77–79]. For example, a study by Bastiaannet et al. investigated the effect of respiratory motion on liver dosimetry for SIRT planning and assessment [80]. Deep respiratory motion with a maximum range of 3 cm was modeled in 4D XCAT liver phantoms containing tumors of different sizes. They found that the RCs and hence the dose estimates decreased on average by 30 % [80]. In addition, a phantom study on ^{18}F-PET/CT observed tumor contrast recovery errors of up to 10% for displacements of 15 mm, highlighting the potential impact of even small patient movements [81]. However, little research has been done on the effects of motion on ^{177}Lu-PSMA SPECT quantification and dosimetry [76]. While longer acquisition times provide higher count statistics and reduced noise, shorter acquisitions times may result in less patient motion. However, the interplay between noise and patient motion on quantitative SPECT for image-based dosimetry has not been quantified yet. Based on the findings, along with comfortable patient positioning, imaging protocols could be further optimized to minimize the impact of patient motion while improving patient comfort and throughput at the same time.

TABLE 2.1: **Literature overview of STP dosimetry for ^{177}Lu-PSMA therapy.** The studies by Brosch-Lenz et al. [53], Jackson et al. [54], Rinscheid et al. [82], Peters et al. [71], Kurth et al. [83] and Karimzadeh et al. [84] vary in reference model and optimum SPECT imaging time points. *PBPK: Physiologically-based pharmacokinetic modeling. Adapted from [66].

Study	**Reference Time Sampling [h]**	**Reference Fit**	**Optimum STP [h]**		
			Kidneys	Lesions	Glands
[53]	24, 48, 72	Mono-exp.	48	72	-
[54]	4, 24, 96	Tri-exp.	$<$48	$\geq$72	$<$48
[82]	0.5-2, 24, 168	PBPK*/Mono-exp.	52	72	-
[71]	1, 24, 48, 72, 168	Linear interpolation and mono-exp.	24/48	168	24/48
[83]	2, 24, 48, 72	Rapid uptake and bi-exp.	48	-	48
[84]	2, 24, 48, 72-168	Mono- or bi-exp.	48	$\geq$72	48

As emphasized by Dieudonné et al., there is a need for more clinical studies to provide evidence of the benefits of dosimetry-guided radioligand therapy [85]. To this end, standardized and clinically feasible dosimetry protocols still need to be established to further integrate robust dosimetry into clinical practice.

In the following, three studies are presented that were performed within the scope of this dissertation and address the aforementioned challenges in dosimetry for ^{177}Lu-PSMA therapy, namely the impact of a late SPECT/CT measurement, STP imaging, and the effects of patient motion combined with scan time reduction.

2.2 Publication 1

The first study included in this thesis, titled *'Investigation of image-based lesion and kidney dosimetry protocols for ^{177}Lu-PSMA-I&T therapy with and without a late SPECT/CT acquisition'*, investigated the impact of late SPECT/CT measurements in clinical dosimetry of lesions and kidneys and at what cost they can be omitted [65].

The study included five prostate cancer patients receiving [^{177}Lu]Lu-PSMA-I&T, for whom a SPECT/CT measurement at 168 h p.i. was available, in addition to the usual three SPECT/CT acquisitions at 24 h, 48 h and 72 h. Using the four measurement time points, the best-fitting models for lesions and kidneys were first determined to be a mono-exponential and a population-based bi-exponential model, respectively. The BED for 43 lesions and 10 kidneys was calculated to serve as a reference for reduced sampling schedules. Figure 2.1 shows an example of a TAC fitted with the mono- and bi-exponential models and reduced sampling schedules with three and two time points (days 1, 2, 3 and days 1, 2). Since the TACs are extrapolated to infinity, even small deviations in the TAC course can cause significant differences in the TIAs. The lowest deviation of lesion BEDs (4 ± 5%) compared to the reference protocol was observed if SPECT acquisitions at days 1, 3, and 7 were considered. To quantify the accuracy of the patient-specific dosimetry of each sampling schedule and fitting model, the relative number of lesions with less than 10 % BED deviation from the reference was evaluated. For the best time sampling (days 1, 3 and 7), 95 % of all deviations were within 10 %. Excluding the late measurement on day 7 and using measurements at days 1, 2 and 3 only resulted in a higher mean deviation of 8 ± 13 %. Most lesion BEDs (70 %) were underestimated, but still 86 % of all deviations were smaller than 10 % and within clinically acceptable ranges. Higher deviations of individual lesion BED values from the ground truth were strongly correlated (r = 0.88) with higher deviations of the lesion effective half-life compared to the expected half-life (average over all lesions of the patient cohort). For the other two possible time samplings based on three SPECT scans (1, 2, 7 and 2, 3, 7), a smaller percentage of lesions showed deviations less than 10 % (67 % and 61 %). For the kidneys, the deviations were generally small, irrespective of the protocol applied, with the lowest median deviation being 0 ± 1 % and a maximum deviation of -2 % for days 1, 2, and 3. The use of only two SPECT/CT measurements resulted in higher mean deviations from the reference. Here, the best combination for both, lesions and kidneys, was the use of measurements at days 1 and 3 resulting in a mean deviation of 10 ± 14 % for the lesions (65 % below 10 %) and 2 ± 2 % for the kidneys.

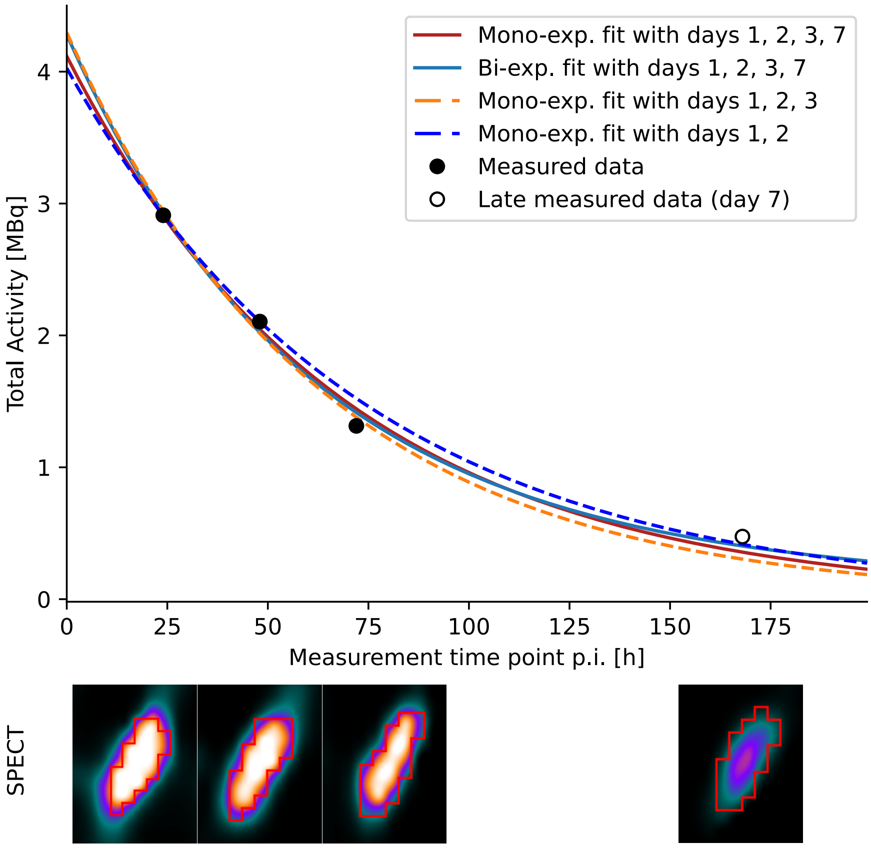

FIGURE 2.1: **Exemplary lesion TAC with different fits and time sampling.** A tumor lesion was segmented with isocontour-based segmentation on each of the four available SPECT measurements at 24, 48, 72 and 168 h after injection. The reference was fitted with a mono- and bi-exponential model and a mono-exponential fit was used to approximate pharmacokinetics with three and two time points.

2.3 Publication 2

In the second study, titled *'Impact of the reference multiple-time-point dosimetry protocol on the validity of single-time-point dosimetry for [^{177}Lu]Lu-PSMA-I&T therapy'*, dosimetry with only one SPECT measurement time point was evaluated [66]. STP dosimetry has gained popularity due to its clinical practicability. However, previous studies have reported different results regarding the optimal method and imaging time point, depending on the reference model used for comparison (see Table 2.1). This publication specifically investigated the impact of the choice of reference multiple time point protocol on the performance of different STP dosimetry methods for [^{177}Lu]Lu-PSMA-I&T therapy [66].

The study included seven patients and a total of 60 lesions, 14 kidneys and 10 submandibular glands were investigated with SPECT/CT acquisition times at 24 h, 48 h, 72 h and 168 h. Differences in goodness-of-fit parameters of mono- and population-based bi-exponential fitting models were relatively small for lesions and kidneys and no clear preference could be deduced. However, the deviations in absorbed dose were significantly different for the two models, with maximum deviations of -44 % for lesions and -19 % for kidneys. Only for the submandibular glands, the population-based bi-exponential model was clearly superior. Three different STP dosimetry methods were evaluated by comparing the absorbed dose calculated with one of the four available SPECT/CT scans to the reference values. The results showed that the best imaging time points varied by compartment: for lesions 72 h p.i., kidneys 48 h p.i. and glands 24 h p.i. were optimal. The choice of the reference protocol influenced the best performing STP dosimetry method and optimum measurement time point, showing the least deviation from the reference absorbed dose. Imaging at 48 h p.i. may serve as a compromise to use one imaging time point for dosimetry across all three compartments. In our patient cohort, deviations from the bi-exponential reference model at 48 h p.i., calculated using the best-performing bi-exponential population-based STP method, were 4 ± 4 % for kidneys, 10 ± 13 % for lesions, and 10 ± 14 % for glands.

2.4 Additional Studies

In the third study, a complementary approach to further improve the efficiency of dosimetry protocols in ^{177}Lu-PSMA therapy by optimizing the measurement duration was investigated. This was motivated by the observation that long scan times lead to a higher likelihood of pain-driven patient motion. Patient motion during the measurement can cause artifacts in the SPECT activity quantification and thus in the dosimetry of lesions and organs-at-risk. Shorter scan times reduce the risk of patient movement, however introduce uncertainty by higher image noise. This study aimed to quantify the impact of patient motion in combination with varying acquisition times per projection during post-therapeutic ^{177}Lu-PSMA SPECT/CT scans on the resulting dosimetry errors.

A patient-like virtual phantom (voxel size of 1 mm^3) was designed to contain two kidneys (100 ml and 138 ml volume) and 21 spherical lesions (5/10/15/25 ml volume) (see Figure 2.2 **a**). SPECT acquisitions were simulated using the Monte Carlo simulation software SIMIND v. 7.0.3 (c.f. Section 1.2.4). The parameters in SIMIND were adjusted to simulate a SPECT acquisition with a Siemens Symbia Intevo SPECT/CT with a medium-energy low-penetration collimator, an emission window at 208 keV and two scatter windows at 170 keV and 240 keV (15 % width). The resulting 128 projections had a pixel size of (0.48 cm)^2 and a matrix size of 128 x 128 pixels. Since the simulation is assumed to be noise free for sufficiently high count statistics (coefficient of variation between voxels in homogeneous background smaller than 10 %), Poisson noise was applied to the projections in order to mimic realistic measurements (see Figure 2.2 **b**). Simulations were performed in two bed positions and for four different measurement time points (24 h, 48 h, 72 h and 168 h p.i.), with lesion, kidney and background activity concentrations derived from five patients from clinical routine therapies. In a pre-study, a suitable parameter space (e.g. motion directions, magnitude, frequency and patterns) was evaluated. As a result, the phantom was shifted by ± (5, 10, 20) mm in the horizontal direction and + (5, 10, 20) mm in the vertical direction, resulting in a total of 112 simulated SPECT/CT acquisitions. A schematic illustration of the SPECT acquisition process is presented in Figure 2.2 **c**. All simulations were performed on the LRZ Linux Cluster. Two acquisition protocols were evaluated: a shorter scan with a step time of 5 s per projection ($\approx$ 11 min total) and a longer scan with a step time of 15 s ($\approx$ 32 min total). To simulate motion, projections acquired for the shifted phantom position were inserted into the baseline projection dataset (i.e., projections simulated for the phantom in the non-displaced position) on average either every 1 or 4 minutes resulting in average times between motion events of $\Delta t_M = 1$ min or $\Delta t_M = 4$ min. If the motion event occurred during a projection, the resulting projection was a weighted mixture of the projections in the two positions, proportional to the time spent in each position. The phantom returned to its original position with a 2/3 probability and remained displaced with a 1/3 probability. Exemplary motion pattern with different absolute phantom shifts are shown in Figure 2.2 **d**. The maximum motion shift which could occur in this configuration was 4 cm. For each parameter combination and measurement time point, 250 projection data sets (N = 4000) with random motion patterns were generated and reconstructed using a MAP-OSEM algorithm (16 subsets, 20 iterations) with a quadratic penalty (Bayesian weight $\beta = 0.001$), scatter and attenuation correction, and Gaussian resolution modeling. Lesions were segmented automatically using a threshold-based approach optimized on motion-free data, while the kidneys were delineated using the input mask, similar to a CT-based segmentation. Figure 2.2 **e** shows reconstruction slices containing three lesions with segmentation. For the calculation of the absorbed dose, the TIA was calculated by fitting and integrating TACs, which were randomly generated using the activity concentrations and volumes from the 250 motion-affected datasets (c.f. Figure 2.2 **f**). Additionally, the density for each VOI was randomly selected from the 250 motion-affected datasets. This process was repeated N = 1000 times, resulting in a distribution of absorbed dose values around the true values, as illustrated exemplarily in Figure 2.2 **g**. The deviations of these motion-influenced absorbed dose ($\mathrm{D_{Motion}}$) values from the motion-free reference data ($\mathrm{D_{Ref}}$) were calculated by

$$\text{Deviation} = \frac{\mathrm{D_{Motion}} - \mathrm{D_{Ref}}}{\mathrm{D_{Ref}}}. \tag{2.1}$$

With deviations between 5 s and 15 s acquisitions following a normal distribution, a paired t-test was performed to determine statistical significance.

Results showed that the motion-induced deviations in absorbed dose were generally larger for the longer 15 s step time and higher motion frequency (Figures 2.3 and 2.4). Across all lesions, the median (min, max) absorbed dose deviation was -16 % (-28 %, -2 %) for 5 s step time and -25 % (-33 %, -7 %) for 15 s step time for $\Delta t_M = 1$ min (see Figure 2.3). For $\Delta t_M = 4$ min, the deviations were smaller: -6 % (-19 %, 2 %) for 5 s step time and -13 % (-20 %, 3 %) for 15 s step time (see Figure 2.4). Deviations for the 5 s step time were significantly lower ($p < 0.05$) compared to the longer step time, irrespective of the motion frequency. Thus, a step time of 5 s per projection would not only be preferable in the context of clinical workload, but can also be implemented to reduce the impact of patient motion.

For the kidneys, absorbed dose deviations were more pronounced in kidney 1, especially for the 15 s step time, where $\Delta t_M = 4$ min resulted in a mean deviation of

-14 ± 9 %, compared to -9 ± 6 % in kidney 2. The greater impact on kidney 1 is likely due to its anatomical location and spillover from adjacent lesions. For 5 s step time and $\Delta t_M = 4$ min, the deviations were -5 ± 4 % in kidney 1 and -3 ± 3 % in kidney 2. For $\Delta t_M = 1$ min, the deviations increased to -19 ± 8 % (kidney 1) and -10 ± 6 % (kidney 2) for 5 s step time and -24 ± 6 % (kidney 1) and -14 ± 5 % (kidney 2) for 15 s step time.

Figures 2.3 and 2.4 illustrate the deviations of each individual lesion and kidney. Lesions 3, 6, 9, and 16 showed high standard deviations despite small mean deviations, even for a lower motion frequency. This indicates that even one motion event during the course of the scan (in the case of 5 s step time and $\Delta t_M = 4$ min) can lead to large quantification errors for some lesions, depending on the lesion's location, influence of surrounding tissue, mismatch between CT and SPECT, volume and foreground-to-background ratio. This is the first study investigating the effects of irregular motion in SPECT-based dosimetry for radionuclide therapy using ^{177}Lu. A manuscript reporting on these findings is in preparation.

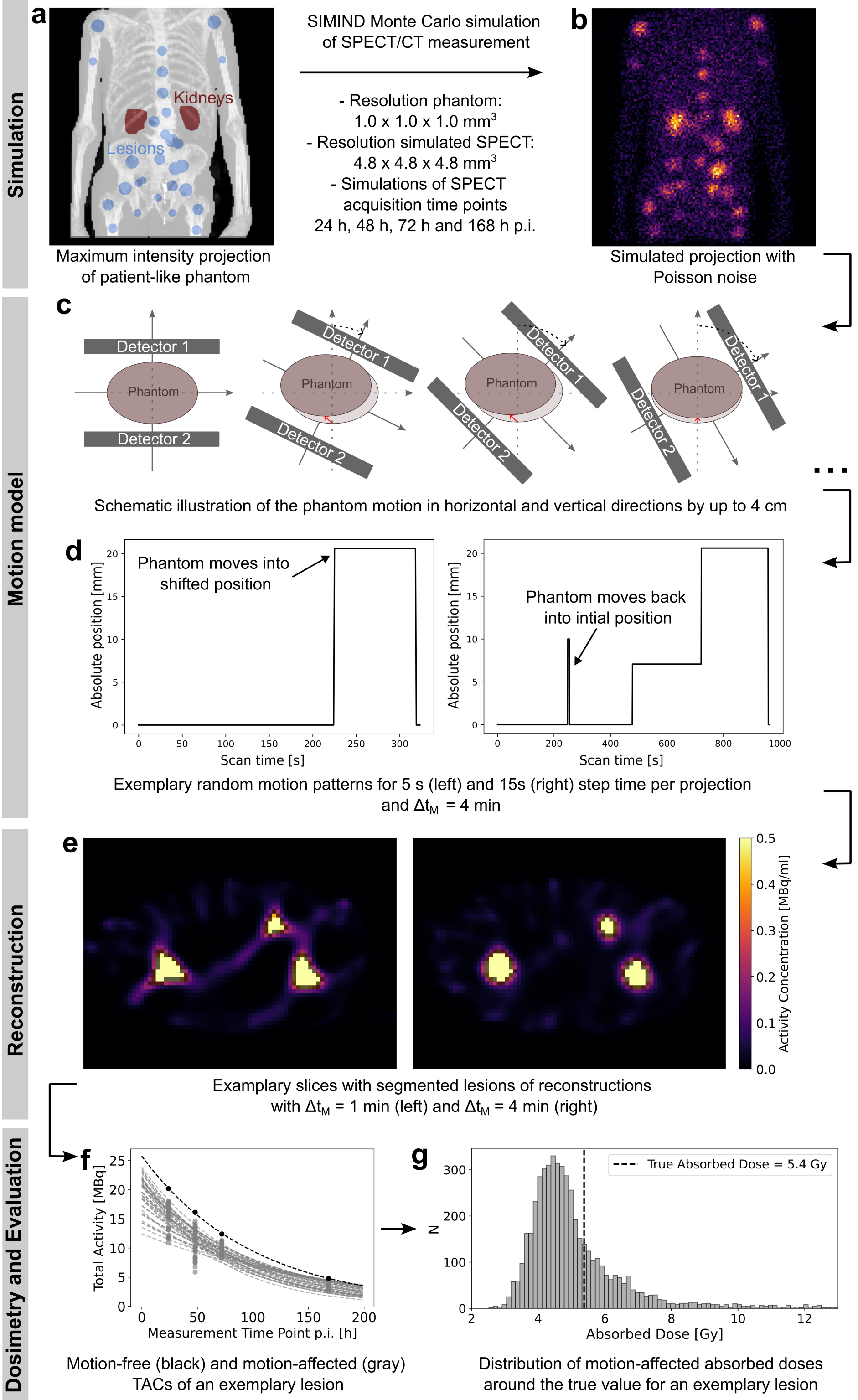

FIGURE 2.2: **Workflow overview.** SPECT projections of a patient-like phantom were simulated using SIMIND (**a**, **b**). A total of 112 simulations were generated, including four different measurement time points and various phantom positions. Motion-affected datasets were created with simulated motion events occurring on average every 1 minute or 4 minutes, using step times of either 5 s or 15 s (**c**, **d**). All datasets were reconstructed, and lesions were segmented using a threshold-based method (**e**). TACs from the motion-affected datasets were analyzed (**f**), leading to absorbed dose estimates that deviated from the true value (**g**).

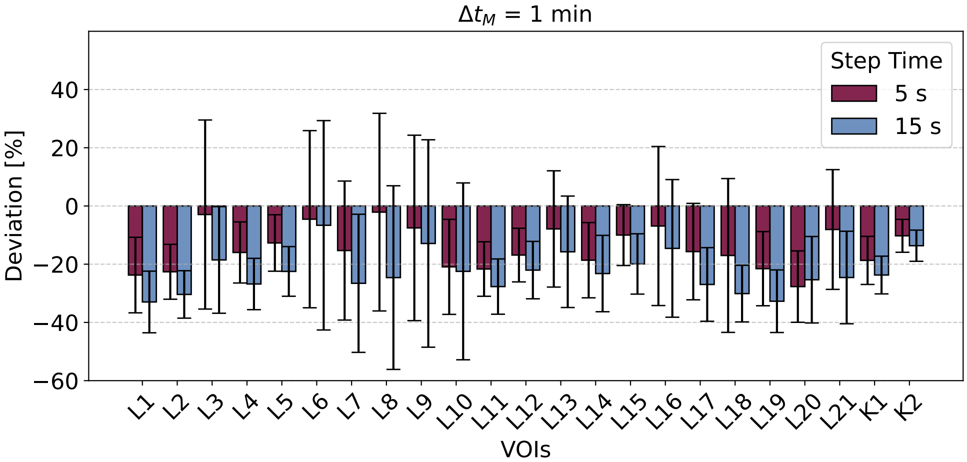

FIGURE 2.3: **Comparison of absorbed dose deviations for 5 s versus 15 s step time and a motion event every 1 min (Δt_M = 1 min).** The deviations of 1000 random realizations from the motion-free ground truth were averaged and plotted for 21 lesions and two kidneys, comparing step times 5 s and 15 s per projection. Error bars represent the standard deviation.

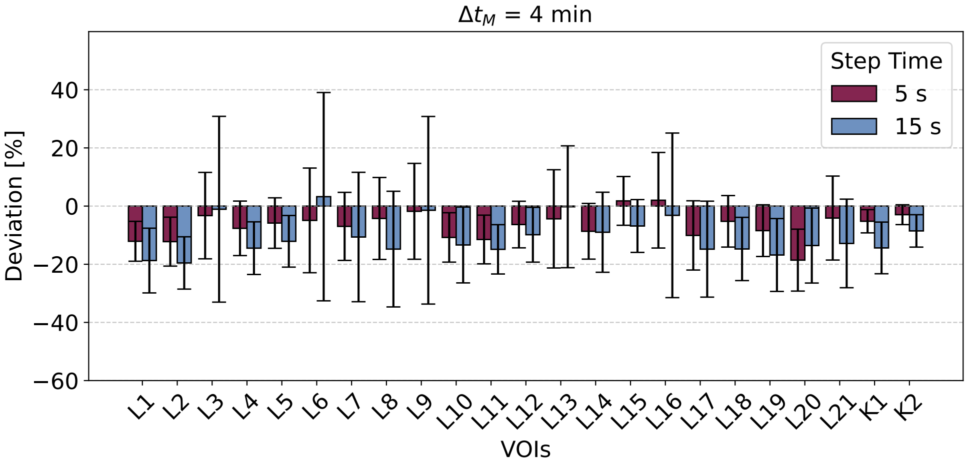

FIGURE 2.4: **Comparison of absorbed dose deviations for 5 s versus 15 s step time and a motion event every 4 min (Δt_M = 4 min).** The deviations of 1000 random realizations from the motion-free ground truth were averaged and plotted for 21 lesions and two kidneys, comparing step times 5 s and 15 s per projection. Error bars represent the standard deviation.

3 | Discussion and Outlook

In the scope of this dissertation, various sources of error in SPECT-based dosimetry for ^{177}Lu-PSMA therapy of metastatic prostate cancer were investigated. The studies primarily investigated the influence of temporal sampling of SPECT/CT acquisitions on the dosimetry of tumors and organs-at-risk, focusing on the inclusion of late imaging time points and the feasibility of using a single acquisition. In case of multi-time-point strategies, the appropriate model for TAC fitting was determined. In addition, the effects of patient motion and measurement duration were analyzed in a simulation study. Based on these results, recommendations for clinical dosimetry protocols for ^{177}Lu-PSMA therapy were derived.

The first study showed that a late SPECT/CT scan on day 7 p.i. can be omitted with a mean BED deviation of 8 ± 13 % over the entire patient cohort. However, for personalized dosimetry, individual outliers are more important. Therefore, it is important to note, that 86 % of the deviations were less than $|10|$ %, which means that for the majority of lesions, the BED can be determined with sufficient accuracy, while the outlier lesions can be identified by an unusually high effective half-life. Thus, a sampling plan with acquisitions on days 1, 2, and 3 represents a compromise between accuracy and clinical feasibility. Rinscheid et al. performed a simulation study to investigate optimal sampling schedules for tumor and renal TIA determination using hybrid planar and SPECT imaging [82]. Although they recommend including a late acquisition at 192 h p.i. for tumor lesions (based on 26 lesions), they found that the root mean squared error of the tumor TIA was still 11 % with all images being acquired within 72 h, i.e. using time points 4, 20, 68 and 72 h [82]. Despite long-term retention is present in lesions, very late measurements are logistically and technically challenging. SPECT/CT scans on day 7 usually have to be performed on an outpatient basis. Further, the decreasing concentrations of the radionuclide lead to a significant increase in image noise and consequently require a prolongation of the measurement duration [86]. For kidneys, which typically present a shorter effective half-live compared to lesions (see Figure 3.1), early activity measurements sufficiently capture the pharmacokinetics and late measurements are not necessary to support the required accuracy of the dose estimates.

Overall, it was observed that the choice of the TAC fitting model can have a greater impact on absorbed dose estimates of individual lesions than the temporal sampling itself, as discussed in Section 2.3. Notably, significant differences in lesion absorbed doses were found between the evaluated mono- and bi-exponential models, with deviations up to -44 %. Given that the number and timing of clinical measurements are inherently limited, it is important to note that even our reference model, which includes four time points over a span of 168 h p.i., represents only an approximation of the true pharmacokinetic behavior.

In agreement with Kurth et al., Peters et al. and Brosch-Lenz et al., a further reduction of the number of SPECT/CT scans by performing STP dosimetry is feasible [53, 71, 83]. STP dosimetry for organs-at-risk, such as the kidneys and salivary glands, showed smaller errors and lower variability in errors compared to tumor lesions. This is primarily attributed to the lower inter-individual variability in organ pharmacokinetics compared to that of lesions, as illustrated in Figure 3.1. More precisely, the coefficient of variation of the effective half-life is more than 10 % higher in lesions than in kidneys. However, STP methods rely on assumptions about pharmacokinetics, and their accuracy especially for lesion dosimetry is limited by the lack of patient-specific time-dependent data. In this study we could show that the optimal imaging time point for STP dosimetry, the optimum STP method and the associated errors varied for reference models and investigated organ. This variability highlights the importance of prioritizing specific compartments in STP protocols based on the clinical objectives and the need for standardization of dosimetry protocols. The imaging time point of 24 h was optimal for salivary glands, 48 h for kidneys, and 72 h for lesions. Multi-time point protocols remain preferable for robust lesion dosimetry.

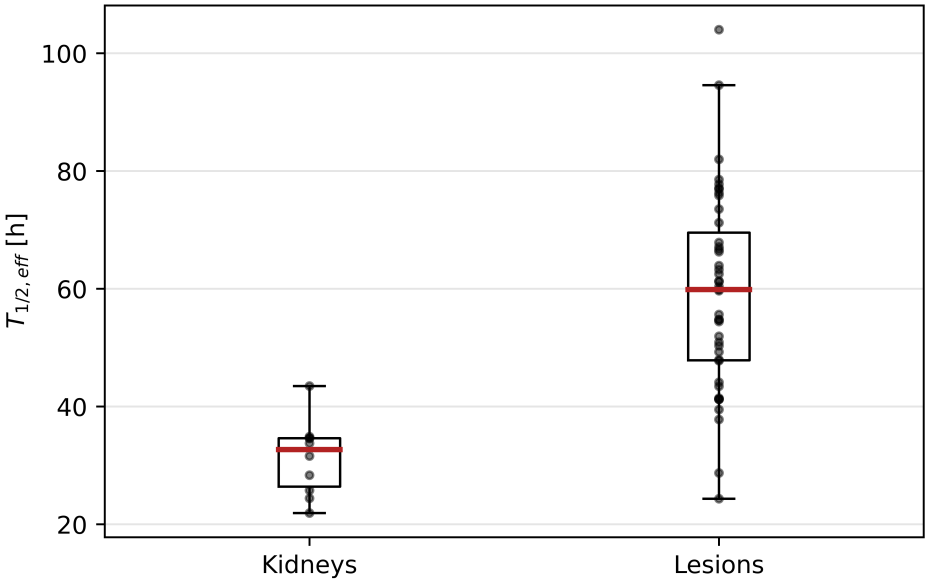

FIGURE 3.1: **Distribution of effective half-life of kidneys versus lesions.** The mean effective half-life of the kidneys is 31 ± 6 h, while for the lesions, the effective half-life is 59 ± 17 h. The coefficient of variation is much higher for the lesions (28 %) than for the kidneys (19 %).

Studies I and II demonstrated that the efficiency of dosimetry protocols can be enhanced through optimized time sampling. An alternative to skipping SPECT/CT measurements would be to decrease the acquisition time per single SPECT/CT examination. Further, the longer a patient is required to remain still, the greater the probability of pain-induced movements, also emphasizing the benefit of shorter acquisition protocols. Thus, an additional study investigated the impact of irregular, pain-induced patient motion on activity quantification and absorbed dose estimation for a long acquisition protocol (15 s step time per projection) and a short protocol (5 s per projection). To investigate this, Monte-Carlo SPECT simulations were conducted using a virtual, patient-like phantom with realistic activity concentrations in lesions and organs. Randomly generated motion patterns were mimicked. When motion occurred on average every minute, maximum absorbed dose deviations reached -28 % for lesions and -19 % for kidneys with the short step time. For the long step time, these deviations increased to -33 % and -24 %, respectively. When the motion frequency was reduced to once every four minutes, the maximum deviations for the long scan duration decreased to -20 % for lesions and -14 % for kidneys, although variability remained high. These results suggest that a shorter acquisition time of 5 s is preferable, as it reduces the likelihood of motion during the scan while improving clinical efficiency. While clinical validation of these findings would be valuable, the simulation study provided a controlled environment to assess motion effects on dosimetry and to test motion correction algorithms. The simulation data can also be adapted to evaluate time dependent motion patterns in future studies.

This dissertation demonstrated that reliable dosimetry can be simplified for easier clinical implementation, particularly for organs-at-risk. These findings could enhance the potential for personalized therapy planning based on dosimetry, moving beyond the conventional one-size-fits-all approach. A phase II trial by Sundlöv et al. assessed the feasibility of a dosimetry-based approach for ^{177}Lu-DOTATATE therapy in patients with neuroendocrine tumors [46]. The number of treatment cycles was individualized based on renal BED estimation utilizing four planar scintigraphies at 4, 24, 48/96 and 168 h p.i. along with one SPECT/CT at 24 h. Treatment continued until a prescribed renal BED of 27 ± 2 Gy (initial step) or 40 ± 2 Gy (in a selected sub-group) was reached. Among 96 patients, 16 % showed partial response, 66 % stable disease, and 19 % experienced progression in a median of 5 cycles (range: 1-9). Median progression-free survival was 29 months, and median overall survival was 47 months. Higher renal BEDs correlated with improved survival, while no cases of severe renal toxicity were reported during the follow-up period. The findings by Sundlöv et al. provide evidence that dosimetry-guided, personalized variable-cycle therapy is safe and effective, and may be superior to fixed-cycle treatments [46]. An alternative approach for individualized treatments involves increasing the prescribed activity per cycle, as explored by Del Prete et al. [87]. In contrast to the conventional administration of a fixed activity in ^{177}Lu-octreotate peptide receptor radionuclide therapy of neuroendocrine tumors, the injected activity per cycle was adjusted for each patient based on renal absorbed doses. The dosimetry protocol comprised three quantitative SPECT/CT measurements at 4, 24 and 72 h after injection. For the first cycle, the injected activity was adapted based on the patient's glomerular filtration rate and body surface area while subsequent cycles were adjusted according to the previously determined renal dose per unit of injected activity (Gy/GBq). Patients received a median injected activity of 8.8 GBq (range 0.7 to 32.4 GBq) per cycle for three to four cycles, leading to a 1.48-fold increase in maximum tumor absorbed dose compared to standard PRRT, without incidence of severe renal toxicity [87]. Assuming that absorbed dose in lesions correlates with clinical outcome, as shown by Völter et al., a promising and feasible strategy for personalized dosimetry-guided therapy aiming for improved efficiency could involve maximizing the absorbed dose in selected index lesions while minimizing absorbed doses to organs-at-risk [50]. However, a suitable method for identifying representative index lesions in pre-therapeutic or post-therapeutic images has yet to be established. Possible strategies might include selecting the lesions with the highest uptake and those with the lowest uptake, or a combination of both.

In addition to the previously discussed sources of error related to limited time-sampling, inaccuracy in TAC fitting models and patient movement, a substantial source of error in SPECT imaging is the limited and distance-dependent spatial resolution of the SPECT system itself. This leads to space-variant and object dependent distortions, resulting in both local over-estimation and under-estimation of reconstructed activity concentrations. These errors in the SPECT/CT images across the different time points not only affect the accuracy of the fitted TACs and the resulting absorbed dose estimates, but also impair reliable image-based object segmentation and volume determination, particularly for small lesions [88].

Further, the limited spatial resolution of nuclear medicine imaging using PET and SPECT, which typically ranges from several millimeters to even centimeters, makes it difficult to study absorbed dose distributions at the microscopic scale. Consequently, research on absorbed dose distributions at the cellular level and the underlying radiobiological effects is still an ongoing process. However, integrating biological effects is crucial for the redefinition of absorbed dose thresholds, which are typically based on data from external beam radiation therapy.

During the past years, promising new developments from researchers and manufacturers for the improvement of quantitative imaging and image-based dosimetry have emerged. Quantitative SPECT/CT imaging for instance may benefit significantly from the utilization of Cadmium Zinc Telluride (CZT) detectors, which have already made their way in a few commercially available SPECT/CT machines. CZT detectors could offer higher sensitivity and energy resolution than conventional Thallium-doped Sodium Iodide detectors, potentially enabling faster image acquisition, higher scanner throughput and patient comfort, while maintaining image quality [89]. Additionally, artificial intelligence (AI) could play a major role, e.g. in noise reduction or the reduction of imaging time through the replacement of real projections by deep-learning based synthetic projections [90]. The post-processing of SPECT/CT data could be accelerated by automatic, AI-powered segmentation tools, which further minimize operator variability [91]. The commercialization of dosimetry software could provide automated absorbed dose calculations and uncertainty estimations, simplifying and enhancing efficient routine dosimetry. Further advancements in STP dosimetry accuracy may be achieved through the application of linear mixed-effects models, which can account for inter-individual variability [92]. Machine learning could also be used for dosimetry by directly predicting individual dosimetry before ^{177}Lu-PSMA therapy, e.g. based on pre-therapy PET imaging and blood values [93]. These innovations hold the potential to make dosimetry more accessible and practical, paving the way for personalized radionuclide therapy with improved patient outcomes and streamlined clinical workflows.

4 Contributions to original publications

This chapter summarizes my contributions to the two original publications on which this cumulative dissertation is based.

4.1 Contributions to Original Publication I

As a prerequisite for the first publication, several parameters related to the acquisition time and reconstruction protocol, as well as a suitable segmentation method for the short measurement time of 5 s per projection had to be evaluated in a preliminary study. Since this short measurement time has not yet been well established in routine clinical dosimetry, thorough validation was required. I evaluated the quantification of SPECT/CT acquisitions with a step time of 5 s and 15 s per projection using measurements of a cylindrical phantom containing six spheres with volumes ranging from 0.5 ml to 26.5 ml (NEMA IEC body phantom). The measurements included various sphere-to-background ratios (16:1, 8:1, and 4:1) and a range of reconstruction settings. Concerning the latter, I assessed the impact of the β-parameter of the intra-reconstruction quadratic penalty (tested at 0.1, 0.01, and 0.001) and the effect of matrix up-sampling. The RCs derived from CT-based segmentation of the spheres and background were calculated across all parameter combinations. In addition, I conducted a literature review on SPECT-based segmentation methods and implemented six different algorithms. These were evaluated across all phantom datasets and reconstruction settings by comparing the segmented volumes and corresponding mean RCs. The best-performing method was identified as a peak-at-max isocontour segmentation approach. To demonstrate clinical feasibility of the pre-defined reconstruction settings for the short acquisition time, I evaluated the RCs using a NEMA phantom measurement with a 16:1 sphere-to-background ratio. The spheres were segmented using both the peak-at-max isocontour segmentation, as applied in the patient SPECT data and a CT-based segmentation method, which serves as the standard for NEMA phantom evaluation. RCs obtained from both methods were compared and visualized. This analysis confirmed that a minimum lesion volume of 5 ml yields acceptable RCs under the evaluated conditions.

In the first publication, five patients with mCRPC treated with [^{177}Lu]Lu-PSMA-I&T were included, who underwent four SPECT/CT scans each. I reconstructed the data using a MAP-OSEM reconstruction algorithm with the previously optimized parameters. For attenuation correction, I co-registered the SPECT and CT scans using the Fusion Tool in the software PMOD version 3.609. Furthermore, I registered the SPECT scans at 48 h, 72 h and 168 h to the 24 h SPECT acquisition. All suitable tumor lesions with a volume larger than 5 ml were segmented in the SPECT images using the adapted peak-at-max isocontour segmentation. Kidneys were segmented manually on the 24 h CT scan. From the SPECT images, I extracted the mean activity concentrations and volumes for all segmented objects and derived densities by converting CT Hounsfield Units (HU) using a pre-defined linear calibration.

The next step involved defining a reference model for dosimetry. I performed a literature review to identify potential fit functions, and selected those proposed by Hardiansyah et al. [94]. I evaluated each of the 18 fit functions based on the sum of squared errors and the coefficient of variation of the fitted parameters. Population-based fits were generated using a Jackknife leave-one-out approach, excluding the lesion under analysis in each iteration. I automated the plotting, fitting, and evaluation using a custom MATLAB script.

To account for biological effects in dosimetry, I investigated the use of BED instead of absorbed dose. As BED modeling in radioligand therapy has not been well established yet, I conducted a literature review to determine relevant radiobiological parameters. Further, I extended the BED calculation to the selected fit functions. I then assessed the impact of reduced sampling schemes by comparing the relative BED deviations from the reference model for both kidneys and lesions. The aim of this approach was to support the development of a dosimetry protocol that remains feasible in clinical practice without requiring late-time point measurements. The analysis showed that high BED deviations can be predicted using the deviation of the lesion's effective half-life from the patient's mean effective half-life.

Based on these findings for [^{177}Lu]Lu-PSMA-I&T, I further evaluated the importance of a day 7 SPECT/CT acquisition in a sub-study involving patients treated with [^{177}Lu]Lu-PSMA-617 to investigate the differences in lesion and kidney absorbed dose values for these two compounds.

I created all figures in the paper using Matlab and Inkscape and wrote the initial manuscript draft, which was then revised by my co-authors. As the corresponding author, I was responsible for the submission and revision process.

4.2 Contributions to Original Publication II

For the second publication, I evaluated seven [^{177}Lu]Lu-PSMA-I&T patients with four SPECT/CT acquisitions. I followed the same workflow as described in Publication I. The developed segmentation method was extended to the submandibular glands. Also, the best-suited reference fit for the salivary glands was evaluated according to the aforementioned criteria, i.e. the sum of squared errors and the coefficient of variation of the fitted parameters. In the next step, a literature research on STP dosimetry methods was performed for ^{177}Lu-PSMA therapies and ^{177}Lu-peptide receptor radionuclide therapy (e.g. ^{177}Lu-DOTATATE). Three methods were defined to calculate the TIA from a single measurement. In the first method, population-based clearance rates were determined and used in mono- or bi-exponential functions to calculate the TIA. A method by Haenscheid et al., originally developed for ^{177}Lu-DOTATATE therapy and a method by Jackson et al., were additionally employed to calculate the TIA [54, 55]. The latter involved the determination of tissue- and time-dependent scaling factors for our patient cohort. The TIA based on STP imaging was assessed for all methods in an automated script and compared to the reference protocol. To determine statistically significant differences, I applied Wilcoxon signed-rank testing. In the publication, I also provided a literature overview over the different reference protocols used in different STP studies. I created all figures in the paper using Python and Inkscape. I wrote the initial draft and was responsible for the submission and the review process of the manuscript.

5 Publications

5.1 Original Publication I

S. Resch, S. Takayama Fouladgar, M. Zacherl, G.T. Sheikh, G. Liubchenko, M. Rumiantcev, L.M. Unterrainer, V. Wenter, P. Bartenstein, S.I. Ziegler, H. Ilhan, L. Beyer, G. Böning, & A. Delker, "Investigation of image-based lesion and kidney dosimetry protocols for ^{177}Lu-PSMA-I&T therapy with and without a late SPECT/CT acquisition", *EJNMMI physics*, vol. 10, no. 1, p. 11, 2023.
`https://doi.org/10.1186/s40658-023-00529-8`

5.2 Original Publication II

S. Resch, S.I. Ziegler, G. Sheikh, L.M. Unterrainer, M.J. Zacherl, P. Bartenstein, Böning G., J. Brosch-Lenz & A. Delker, "Impact of the Reference Multiple-Time-Point Dosimetry Protocol on the Validity of Single-Time-Point Dosimetry for ^{177}Lu-PSMA-I&T Therapy", *Journal of Nuclear Medicine*, vol. 65, no. 8, pp. 1272–1278, 2024.
`https://doi.org/10.2967/jnumed.123.266871`

6 | Bibliography

[1] E. J. Schafer *et al.*, “Recent patterns and trends in global prostate cancer incidence and mortality: An update”, *European Urology*, 2024, ISSN: 0302-2838.

[2] L. Wang, B. Lu, M. He, Y. Wang, Z. Wang, and L. Du, “Prostate cancer incidence and mortality: Global status and temporal trends in 89 countries from 2000 to 2019”, *Frontiers in Public Health*, vol. 10, p. 811 044, 2022.

[3] O. Sartor *et al.*, “Lutetium-177–psma-617 for metastatic castration-resistant prostate cancer”, *New England Journal of Medicine*, vol. 385, no. 12, pp. 1091–1103, 2021.

[4] D. A. Silver, I. Pellicer, W. R. Fair, W. Heston, and C. Cordon-Cardo, “Prostate-specific membrane antigen expression in normal and malignant human tissues.”, *Clinical cancer research: an official journal of the American Association for Cancer Research*, vol. 3, no. 1, pp. 81–85, 1997.

[5] PubChem, *PSMA-617 lu-177*, `https://pubchem.ncbi.nlm.nih.gov/compound/PSMA-617-Lu-177`, Accessed: 2025-1-27.

[6] A. Dash, M. R. A. Pillai, and F. F. Knapp, “Production of 177 lu for targeted radionuclide therapy: Available options”, *Nuclear medicine and molecular imaging*, vol. 49, pp. 85–107, 2015.

[7] M. Riveira-Martin *et al.*, “Radiation exposure assessment of nuclear medicine staff administering [177lu] lu-dota-tate with active and passive dosimetry”, *EJNMMI physics*, vol. 10, no. 1, p. 70, 2023.

[8] U. Hennrich and M. Eder, “[177lu] lu-psma-617 (pluvictotm): The first fda-approved radiotherapeutical for treatment of prostate cancer”, *Pharmaceuticals*, vol. 15, no. 10, p. 1292, 2022.

[9] *Pluvicto*, `https://www.ema.europa.eu/en/medicines/human/EPAR/pluvicto`, Accessed: 2025-04-15.

[10] S. Houshmand, C. Lawhn-Heath, and S. Behr, “Psma pet imaging in the diagnosis and management of prostate cancer”, *Abdominal Radiology*, vol. 48, no. 12, pp. 3610–3623, 2023.

[11] D. Nuklearmedizin, *Therapie mit lu-177 psma, dosimetrie und nachsorge beim metastasierten kastrations-resistenten prostatakarzinom*, 2016.

[12] T. Wollenweber *et al.*, “Renal and salivary gland functions after three cycles of psma-617 therapy every four weeks in patients with metastatic castration-resistant prostate cancer”, *Current Oncology*, vol. 28, no. 5, pp. 3692–3704, 2021.

[13] S. Mahajan, R. K. Grewal, K. P. Friedman, H. Schöder, and N. Pandit-Taskar, “Assessment of salivary gland function after 177lu-psma radioligand therapy:

Current concepts in imaging and management", *Translational Oncology*, vol. 21, p. 101 445, 2022, ISSN: 1936-5233.

[14] C. Kratochwil *et al.*, "Joint eanm/snmmi procedure guideline for the use of 177lu-labeled psma-targeted radioligand-therapy (177lu-psma-rlt)", *European journal of nuclear medicine and molecular imaging*, vol. 50, no. 9, pp. 2830–2845, 2023.

[15] D. S. O'Keefe, D. J. Bacich, and W. D. Heston, "Comparative analysis of prostate-specific membrane antigen (psma) versus a prostate-specific membrane antigen-like gene", *The Prostate*, vol. 58, no. 2, pp. 200–210, 2004.

[16] F. Rosar *et al.*, "Comparison of different methods for post-therapeutic dosimetry in [177lu] lu-psma-617 radioligand therapy", *EJNMMI physics*, vol. 8, no. 1, p. 40, 2021.

[17] G. L. ZENG, J. R. GALT, M. N. WERNICK, R. A. MINTZER, and J. N. AARSVOLD, "Chapter 7 - single-photon emission computed tomography", in *Emission Tomography*, M. N. Wernick and J. N. Aarsvold, Eds., San Diego: Academic Press, 2004, pp. 127–152, ISBN: 978-0-12-744482-6.

[18] W. Schlegel, C. Karger, and O. Jäkel, *Medizinische Physik: Grundlagen – Bildgebung – Therapie – Technik*. Springer Berlin Heidelberg, 2018, pp. 378–379, ISBN: 9783662548004.

[19] T. E. Peterson and L. R. Furenlid, "Spect detectors: The anger camera and beyond", *Physics in Medicine & Biology*, vol. 56, no. 17, R145, 2011.

[20] B. F. Hutton, "Spect imaging: Basics and new trends", in *Handbook of Particle Detection and Imaging*, Springer, 2021, pp. 1217–1236.

[21] H. Krieger, *Grundlagen der Strahlungsphysik und des Strahlenschutzes*. Springer, 2007, vol. 2.

[22] Y. K. Dewaraja *et al.*, "Mird pamphlet no. 23: Quantitative spect for patient-specific 3-dimensional dosimetry in internal radionuclide therapy", *Journal of Nuclear Medicine*, vol. 53, no. 8, pp. 1310–1325, 2012, ISSN: 0161-5505.

[23] J. Leube *et al.*, "Position dependence of recovery coefficients in 177lu-spect/ct reconstructions–phantom simulations and measurements", *EJNMMI physics*, vol. 11, no. 1, p. 52, 2024.

[24] R. S. Lawson, "Gamma camera spect", in *Practical SPECT/CT in Nuclear Medicine*, D. W. Jones, P. Hogg, and E. Seeram, Eds. London: Springer London, 2013, pp. 47–75, ISBN: 978-1-4471-4703-9.

[25] B. F. Hutton, I. Buvat, and F. J. Beekman, "Review and current status of spect scatter correction", *Physics in Medicine & Biology*, vol. 56, no. 14, R85, 2011.

[26] D. Bailey, I. A. E. Agency, J. Humm, A. Todd-Pokropek, and A. Van Aswegen, *Nuclear Medicine Physics: A Handbook for Teachers and Students* (Non-serial publication). International Atomic Energy Agency, 2015, pp. 479–494, ISBN: 9789201438102.

[27] T. Kangasmaa, A. Sohlberg, and J. T. Kuikka, "Reduction of collimator correction artefacts with bayesian reconstruction in spect", *International journal of molecular imaging*, vol. 2011, no. 1, p. 630 813, 2011.

[28] W. Grootjans, A. P. Meeuwis, C. H. Slump, L.-F. de Geus-Oei, M. Gotthardt, and E. P. Visser, "Performance of 3dosem and map algorithms for reconstruct-

ing low count spect acquisitions", *Zeitschrift für Medizinische Physik*, vol. 26, no. 4, pp. 311–322, 2016, ISSN: 0939-3889.

[29] M. Ravi, A. Sewa, T. Shashidhar, and S. S. S. Sanagapati, "Fpga as a hardware accelerator for computation intensive maximum likelihood expectation maximization medical image reconstruction algorithm", *IEEE Access*, vol. 7, pp. 111 727–111 735, 2019.

[30] M. Ljungberg, A. Celler, M. W. Konijnenberg, K. F. Eckerman, Y. K. Dewaraja, and K. Sjögreen-Gleisner, "Mird pamphlet no. 26: Joint eanm/mird guidelines for quantitative 177lu spect applied for dosimetry of radiopharmaceutical therapy", *Journal of nuclear medicine*, vol. 57, no. 1, pp. 151–162, 2016.

[31] J. Zeintl, A. H. Vija, A. Yahil, J. Hornegger, and T. Kuwert, "Quantitative accuracy of clinical 99mtc spect/ct using ordered-subset expectation maximization with 3-dimensional resolution recovery, attenuation, and scatter correction", *Journal of Nuclear Medicine*, vol. 51, no. 6, pp. 921–928, 2010.

[32] S. C. Moore, S. Southekal, M.-A. Park, S. J. McQuaid, M. F. Kijewski, and S. P. Muller, "Improved regional activity quantitation in nuclear medicine using a new approach to correct for tissue partial volume and spillover effects", *IEEE transactions on medical imaging*, vol. 31, no. 2, pp. 405–416, 2011.

[33] J. Tran-Gia and M. Lassmann, "Optimizing image quantification for 177lu spect/ct based on a 3d printed 2-compartment kidney phantom", *Journal of Nuclear Medicine*, vol. 59, no. 4, pp. 616–624, 2018.

[34] K. Erlandsson, I. Buvat, P. H. Pretorius, B. A. Thomas, and B. F. Hutton, "A review of partial volume correction techniques for emission tomography and their applications in neurology, cardiology and oncology", *Physics in Medicine & Biology*, vol. 57, no. 21, R119, 2012.

[35] Y. Liu, Z. Lu, G. Chen, K. Shi, and G. S. Mok, "Partial volume correction for lu-177-psma spect", *EJNMMI physics*, vol. 11, no. 1, p. 93, 2024.

[36] J. Leube, J. Gustafsson, M. Lassmann, M. Salas-Ramirez, and J. Tran-Gia, "A deep-learning–based partial-volume correction method for quantitative 177lu spect/ct imaging", *Journal of Nuclear Medicine*, vol. 65, no. 6, pp. 980–987, 2024.

[37] M. Jalilifar, M. Sadeghi, A. Emami-Ardekani, K. Geravand, and P. Geramifar, "Quantifying partial volume effect in spect and planar imaging: Optimizing region of interest for activity concentration estimation in different sphere sizes", *Nuclear Medicine Communications*, vol. 45, no. 6, pp. 487–498, 2024.

[38] M. B. Toossi, J. P. Islamian, M Momennezhad, M Ljungberg, and S. Naseri, "Simind monte carlo simulation of a single photon emission ct", *Journal of Medical Physics*, vol. 35, no. 1, pp. 42–47, 2010.

[39] M. Ljungberg and S.-E. Strand, "A monte carlo program for the simulation of scintillation camera characteristics", *Computer Methods and Programs in Biomedicine*, vol. 29, no. 4, pp. 257–272, 1989, ISSN: 0169-2607.

[40] `https://eur-lex.europa.eu/legal-content/DE/TXT/PDF/?uri=CELEX:32013L0059`, Accessed: 2025-02-04.

[41] C. Burgard *et al.*, "Tumor sink effect with prostate-specific membrane antigen-targeted theranostics in patients with metastatic castration-resistant prostate cancer: Intra-individual evaluations", *Cancers*, vol. 15, no. 9, p. 2592, 2023.

[42] S. Ha, Y.-i. Kim, J. S. Oh, C. Yoo, B.-Y. Ryoo, and J.-S. Ryu, "Prediction of [177lu] lu-dota-tate therapy response using the absorbed dose estimated from [177lu] lu-dota-tate spect/ct in patients with metastatic neuroendocrine tumour", *EJNMMI physics*, vol. 11, no. 1, p. 14, 2024.

[43] U. Garske-Román *et al.*, "Prospective observational study of 177 lu-dota-octreotate therapy in 200 patients with advanced metastasized neuroendocrine tumours (nets): Feasibility and impact of a dosimetry-guided study protocol on outcome and toxicity", *European journal of nuclear medicine and molecular imaging*, vol. 45, pp. 970–988, 2018.

[44] K. Herrmann *et al.*, "Renal and multiorgan safety of 177lu-psma-617 in patients with metastatic castration-resistant prostate cancer in the vision dosimetry substudy", *Journal of Nuclear Medicine*, vol. 65, no. 1, pp. 71–78, 2024, ISSN: 0161-5505.

[45] M. Sandström, U. Garske-Román, S. Johansson, D. Granberg, A. Sundin, and N. Freedman, "Kidney dosimetry during 177lu-dotatate therapy in patients with neuroendocrine tumors: Aspects on calculation and tolerance", *Acta Oncologica*, vol. 57, no. 4, pp. 516–521, 2018.

[46] A. Sundlöv *et al.*, "Phase ii trial demonstrates the efficacy and safety of individualized, dosimetry-based 177lu-dotatate treatment of net patients", *European journal of nuclear medicine and molecular imaging*, vol. 49, no. 11, pp. 3830–3840, 2022.

[47] M. G. Stabin, R. B. Sparks, and E. Crowe, "Olinda/exm: The second-generation personal computer software for internal dose assessment in nuclear medicine", *Journal of nuclear medicine*, vol. 46, no. 6, pp. 1023–1027, 2005.

[48] M. Chauvin *et al.*, "Opendose: Open-access resource for nuclear medicine dosimetry", *Journal of Nuclear Medicine*, vol. 61, no. 10, pp. 1514–1519, 2020.

[49] C. Meyer, D. Mirando, T. Adams, J. Czernin, J. Calais, and M. Dahlbom, *Patient-specific tumor dosimetry in mcrpc patients treated with 177lu-psma-617*, 2021.

[50] F. Völter *et al.*, "Correlation of an index-lesion-based spect dosimetry method with mean tumor dose and clinical outcome after 177lu-psma-617 radioligand therapy", *Diagnostics*, vol. 11, no. 3, 2021, ISSN: 2075-4418.

[51] K. Sjögreen Gleisner *et al.*, "Eanm dosimetry committee recommendations for dosimetry of 177lu-labelled somatostatin-receptor-and psma-targeting ligands", *European journal of nuclear medicine and molecular imaging*, vol. 49, no. 6, pp. 1778–1809, 2022.

[52] A. Piranfar *et al.*, "Radiopharmaceutical transport in solid tumors via a 3-dimensional image-based spatiotemporal model", *npj Systems Biology and Applications*, vol. 10, no. 1, p. 39, 2024.

[53] J. Brosch-Lenz *et al.*, "Toward single-time-point image-based dosimetry of 177lu-psma-617 therapy", *Journal of Nuclear Medicine*, vol. 64, no. 5, pp. 767–774, 2023.

[54] P. A. Jackson, M. S. Hofman, R. J. Hicks, M. Scalzo, and J. Violet, "Radiation dosimetry in 177lu-psma-617 therapy using a single posttreatment spect/ct scan: A novel methodology to generate time-and tissue-specific dose factors", *Journal of Nuclear Medicine*, vol. 61, no. 7, pp. 1030–1036, 2020.

[55] H. Hänscheid, C. Lapa, A. K. Buck, M. Lassmann, and R. A. Werner, "Dose mapping after endoradiotherapy with 177lu-dotatate/dotatoc by a single measurement after 4 days", *Journal of Nuclear Medicine*, vol. 59, no. 1, pp. 75–81, 2018.

[56] P. Maier, L. Hartmann, F. Wenz, and C. Herskind, "Cellular pathways in response to ionizing radiation and their targetability for tumor radiosensitization", *International journal of molecular sciences*, vol. 17, no. 1, p. 102, 2016.

[57] G. Borrego-Soto, R. Ortiz-López, and A. Rojas-Martínez, "Ionizing radiation-induced dna injury and damage detection in patients with breast cancer", *Genetics and molecular biology*, vol. 38, pp. 420–432, 2015.

[58] W. Hur and S. K. Yoon, "Molecular pathogenesis of radiation-induced cell toxicity in stem cells", *International journal of molecular sciences*, vol. 18, no. 12, p. 2749, 2017.

[59] W. E. Bolch, K. F. Eckerman, G. Sgouros, and S. R. Thomas, "Mird pamphlet no. 21: A generalized schema for radiopharmaceutical dosimetry—standardization of nomenclature", *Journal of Nuclear Medicine*, vol. 50, no. 3, pp. 477–484, 2009.

[60] H. Murshed, *Fundamentals of radiation oncology: physical, biological, and clinical aspects.* Elsevier, 2024.

[61] M. Konijnenberg, "From imaging to dosimetry and biological effects", *Quarterly Journal of Nuclear Medicine and Molecular Imaging*, vol. 55, no. 1, p. 44, 2011.

[62] R. Dale, "Dose-rate effects in targeted radiotherapy", *Physics in Medicine & Biology*, vol. 41, no. 10, p. 1871, 1996.

[63] B. W. Wessels *et al.*, "Mird pamphlet no. 20: The effect of model assumptions on kidney dosimetry and response—implications for radionuclide therapy", *Journal of Nuclear Medicine*, vol. 49, no. 11, pp. 1884–1899, 2008, ISSN: 0161-5505.

[64] B. Jones, R. Dale, C Deehan, K. Hopkins, and D. Morgan, "The role of biologically effective dose (bed) in clinical oncology", *Clinical oncology*, vol. 13, no. 2, pp. 71–81, 2001.

[65] S. Resch *et al.*, "Investigation of image-based lesion and kidney dosimetry protocols for 177lu-psma-i&t therapy with and without a late spect/ct acquisition", *EJNMMI physics*, vol. 10, no. 1, p. 11, 2023.

[66] S. Resch *et al.*, "Impact of the reference multiple-time-point dosimetry protocol on the validity of single-time-point dosimetry for [177lu] lu-psma-i&t therapy", *Journal of Nuclear Medicine*, vol. 65, no. 8, pp. 1272–1278, 2024.

[67] M. S. Hofman *et al.*, "[177lu]-psma-617 radionuclide treatment in patients with metastatic castration-resistant prostate cancer (lupsma trial): A single-centre, single-arm, phase 2 study", *The Lancet Oncology*, vol. 19, no. 6, pp. 825–833, 2018.

[68] S. M. Peters *et al.*, "Intra-therapeutic dosimetry of [177 lu] lu-psma-617 in low-volume hormone-sensitive metastatic prostate cancer patients and correlation with treatment outcome", *European journal of nuclear medicine and molecular imaging*, pp. 1–10, 2022.

[69] *Fda approves novartis radioligand therapy pluvicto® for earlier use before chemotherapy in psma-positive metastatic castration-resistant prostate cancer*, `https://www.novartis.com/us-en/news/media-releases/fda-approves-`

`novartis-radioligand-therapy-pluvicto-earlier-use-chemotherapy-psma-positive-metastatic-castration-resistant-prostate-cancer?`, Accessed: 2025-04-01.

[70] J Kurth, B. Krause, S. Schwarzenböck, L Stegger, M Schäfers, and K Rahbar, "External radiation exposure, excretion, and effective half-life in 177 lu-psma-targeted therapies", *EJNMMI research*, vol. 8, pp. 1–11, 2018.

[71] S. M. Peters *et al.*, "Optimization of the radiation dosimetry protocol in lutetium-177-psma therapy: Toward clinical implementation", *EJNMMI research*, vol. 13, no. 1, p. 6, 2023.

[72] S. Okamoto *et al.*, "Radiation dosimetry for 177lu-psma i&t in metastatic castration-resistant prostate cancer: Absorbed dose in normal organs and tumor lesions", *Journal of Nuclear Medicine*, vol. 58, no. 3, pp. 445–450, 2017, ISSN: 0161-5505.

[73] K. Herrmann *et al.*, "Renal and multiorgan safety of 177lu-psma-617 in patients with metastatic castration-resistant prostate cancer in the vision dosimetry substudy", *Journal of Nuclear Medicine*, vol. 65, no. 1, pp. 71–78, 2024.

[74] J.-M. Beauregard, M. S. Hofman, J. M. Pereira, P. Eu, and R. J. Hicks, "Quantitative 177lu spect (qspect) imaging using a commercially available spect/ct system", *Cancer Imaging*, vol. 11, no. 1, p. 56, 2011.

[75] E. Archer Goode, N. Wang, and J. Munkley, "Prostate cancer bone metastases biology and clinical management", *Oncology Letters*, vol. 25, no. 4, pp. 1–18, 2023.

[76] A. Z. Kyme and R. R. Fulton, "Motion estimation and correction in spect, pet and ct", *Physics in Medicine & Biology*, vol. 66, no. 18, 18TR02, 2021.

[77] G. M. Currie and J. M. Wheat, "The impact of acquisition protocol on the incidence of patient motion in 99mtc based myocardial perfusion spect", *Nuclear medicine communications*, vol. 25, no. 12, pp. 1191–1195, 2004.

[78] J. M. Wheat and G. M. Currie, "Impact of patient motion on myocardial perfusion spect diagnostic integrity: Part 2", *Journal of nuclear medicine technology*, vol. 32, no. 3, pp. 158–163, 2004.

[79] M. Santoro *et al.*, "A novel tool for motion-related dose inaccuracies reduction in 99mtc-maa spect/ct images for sirt planning", *Physica Medica*, vol. 98, pp. 98–112, 2022.

[80] R. Bastiaannet, M. A. Viergever, and H. W. De Jong, "Impact of respiratory motion and acquisition settings on spect liver dosimetry for radioembolization", *Medical physics*, vol. 44, no. 10, pp. 5270–5279, 2017.

[81] K. C. McCall, D. L. Barbee, M. W. Kissick, and R. Jeraj, "Pet imaging for the quantification of biologically heterogeneous tumours: Measuring the effect of relative position on image-based quantification of dose-painting targets", *Physics in Medicine & Biology*, vol. 55, no. 10, p. 2789, 2010.

[82] A. Rinscheid, P. Kletting, M. Eiber, A. J. Beer, and G. Glatting, "Influence of sampling schedules on [177 lu] lu-psma dosimetry", *EJNMMI physics*, vol. 7, pp. 1–14, 2020.

[83] J. Kurth *et al.*, "Streamlined schemes for dosimetry of 177lu-labeled psma targeting radioligands in therapy of prostate cancer", *Cancers*, vol. 13, no. 15, p. 3884, 2021.

[84] A. Karimzadeh *et al.*, "Organ and tumor dosimetry including method simplification for [177lu] lu-psma-i&t for treatment of metastatic castration resistant prostate cancer", *EJNMMI physics*, vol. 11, no. 1, p. 63, 2024.

[85] A. Dieudonné *et al.*, "Dosimetry for targeted radionuclide therapy in routine clinical practice: Experts advice vs. clinical evidence", *European Journal of Nuclear Medicine and Molecular Imaging*, vol. 51, no. 4, pp. 947–950, 2024.

[86] K. S. Gleisner *et al.*, "Long-term retention of 177lu/177mlu-dotatate in patients investigated by γ-spectrometry and γ-camera imaging", *Journal of Nuclear Medicine*, vol. 56, no. 7, pp. 976–984, 2015.

[87] M. Del Prete *et al.*, "Personalized 177 lu-octreotate peptide receptor radionuclide therapy of neuroendocrine tumours: Initial results from the p-prrt trial", *European journal of nuclear medicine and molecular imaging*, vol. 46, pp. 728–742, 2019.

[88] Z. Cheng, P. Chen, and J. Yan, "A review of state-of-the-art resolution improvement techniques in spect imaging", *EJNMMI physics*, vol. 12, no. 1, p. 9, 2025.

[89] V. Nuttens, G. Schramm, Y. D'Asseler, and M. Koole, "Comparison of a 3d czt and conventional spect/ct system for quantitative lu-177 spect imaging", *EJNMMI physics*, vol. 11, no. 1, p. 29, 2024.

[90] J. Leube, J. Gustafsson, M. Lassmann, M. Salas-Ramirez, and J. Tran-Gia, "Analysis of a deep learning-based method for generation of spect projections based on a large monte carlo simulated dataset", *EJNMMI physics*, vol. 9, no. 1, p. 47, 2022.

[91] J. Wasserthal *et al.*, "Totalsegmentator: Robust segmentation of 104 anatomic structures in ct images", *Radiology: Artificial Intelligence*, vol. 5, no. 5, 2023.

[92] D. Hardiansyah, A. Riana, A. J. Beer, and G. Glatting, "Single-time-point dosimetry using model selection and nonlinear mixed-effects modelling: A proof of concept", *EJNMMI physics*, vol. 10, no. 1, p. 12, 2023.

[93] S. Xue *et al.*, "Application of machine learning to pretherapeutically estimate dosimetry in men with advanced prostate cancer treated with 177lu-psma i&t therapy", *European journal of nuclear medicine and molecular imaging*, vol. 49, no. 12, pp. 4064–4072, 2022.

[94] D. Hardiansyah *et al.*, "A population-based method to determine the time-integrated activity in molecular radiotherapy", *EJNMMI physics*, vol. 8, pp. 1–13, 2021.

List of Figures

Danksagung

Zuerst möchte ich mich bei meinem Doktorvater, Prof. Dr. rer. nat. Guido Böning bedanken. Er hat mir die Chance gegeben, in der Nuklearmedizin zu promovieren und mich während dieser Zeit stets unterstützt. Seine offene Bürotür – und damit auch sein offenes Ohr – waren für mich von unschätzbarem Wert. Mit seinen zahlreichen Ideen, seiner Hilfsbereitschaft, seiner Programmierexpertise und seiner motivierenden Art hat er eine sehr entspannte und motivierende Arbeitsatmosphäre geschaffen. Zudem bin ich immer noch dankbar für die Einladung zum Schweinebratenessen, durch die ich meinen ersten (!) Schweinebraten probieren konnte.

Ein ebenso großes Dankeschön gilt auch Dr. rer. nat. Astrid Delker, die mich mit bester Betreuung durch meine Doktorarbeit geführt hat. Astrid hat uns von Anfang an in allen Belangen unterstützt, hatte unzählige Projektideen und immer eine Lösung für unsere Probleme und Fragen parat. Mit ihrer guten Laune und positiven Art ist sie die treibende Kraft in unserer Dosimetriegruppe und für mich nicht nur eine Mentorin sondern auch ein Vorbild.

Mein Dank gilt ebenfalls Prof. Dr. rer. nat. Sibylle Ziegler, die mir ebenfalls mit Rat und Tat zur Seite stand. Durch ihre wöchentlichen Besprechungen und Journalclubs konnte ich viel Neues in der Nuklearmedizin lernen und von ihrem unendlichen Wissen profitieren. Ihre blitzschnellen und unglaublich wertvollen Korrekturen meiner Abstract- und Paperdrafts haben mir sehr geholfen. Auch sie war und ist für mich ein großes Vorbild.

Ein herzlicher Dank geht auch an Prof. Dr. med. Peter Bartenstein, Prof. Dr. med. Dr. rer. biol. hum. Matthias Brendel und Prof. Dr. med. Rudolf Werner, die es mir ermöglicht haben in der Nuklearmedizin zu promovieren und meine MPE-Ausbildung zu machen. Dank ihnen konnte ich an zahlreichen Kongressen teilnehmen, was mich in meiner wissenschaftlichen Ausbildung sehr bereichert hat.

Mein besonderer Dank gilt auch der Physik im Allgemeinen, insbesondere Dr. rer. nat. Christian Zach, der auf jede Frage eine Antwort und bei jedem Problem eine Lösung wusste und Ulrich Geschwendt, der uns mit viel Geduld die klinischen Aufgaben für den MPE gezeigt hat und uns stets hilfsbereit unterstützt hat. Ein großes Dankeschön auch an Angelica, die mir mit ihrer unfassbaren Hilfsbereitschaft und positiven Art bei so manchen Problemchen zur Seite stand und unsere Gruppe sehr bereichert (Mille grazie per tutto!).

Ein großes Danke auch an Christian Gastinger und Tim Bocher, die mir stets bei allen IT-Problemen super schnell geholfen haben.

Ein großes Dankeschön auch an die Ärzte in der Abteilung, insbesondere an Dr. med. Mathias Zacherl und Dr. med. Gabriel Sheikh, die mit ihrem medizinischen Wissen immer weitergeholfen haben.

Meinen beiden Büronachbarn und Kollegen, Mikhail und Grigory, möchte ich ebenfalls für die schöne Zusammenarbeit danken. Ich bin sehr dankbar, dass wir alle Herausforderungen und neuen Aufgaben zusammen lernen und meistern konnten und sie mir bei allen Problemen stets hilfsbereit zur Seite standen.

Mein Dank geht auch an das gesamte Team der Nuklearmedizin, das mich während meiner Promotionszeit begleitet hat.

Ein besonderer Dank gilt meinen Mädels - Lea, Isabelle, Rebecca, Marlies und Manvir - mit denen ich durch Hochs und Tiefs gehen konnte und die jeden Tag dafür gesorgt haben, dass ich mich auf die Arbeit freue. Ich bin unfassbar dankbar, euch in meinem Leben zu haben.

Ein ganz besonderer Dank gilt meiner Freundin Rabea, die seit dem Studium an meiner Seite war und mit mir – nur eine Abteilung weiter – dieselben Höhen und Tiefen durchlebt hat. Ich bin unfassbar dankbar für deine Freundschaft und hoffe, wir können weiterhin Seite an Seite durchs Leben gehen.

Meinen Eltern bin ich unendlich dankbar für ihre beständige Unterstützung und dafür, dass sie in schwierigen wie in schönen Momenten stets mitgefiebert und sich mit mir gefreut haben.

Schließlich danke ich von Herzen meinem Freund Franz, der jede Herausforderung und jede Freude dieser Zeit mit mir geteilt und mich immer unterstützt hat. Ohne ihn wäre dieser Weg um einiges schwerer gewesen.

Danke.